6.2 Methodology

6.2.1 Design of experiments

The unit cell geometry chosen for this study is the extensively used Body Centered Cubic (BCC), see Figure 6.3a. This geometry present some advantages like a improved printability due to the lack of horizontal struts and its simplicity as all the struts forming the unit cell present the same orientation. The selected CAD strut thickness was 0.6 mm and the unit cell size was set to 3 x 3 x 3 mm. With this unit cell as foundational element, 10 x 10 x 15 mm lattice structures were designed (see Figure 6.3b). Two 10 x 10 x 2.5 mm caps were added at the bottom and top of the lattice structure to improve contact between the clamps and the lattice structure during thermomechanical testing. All samples in the study were printed vertically, perpendicular to the baseplate as indicated in Figure 6.3b. The NiTi powder used in this chapter is the same as that used in Chapter 3. The same building conditions detailed in Chapter 3 were used to manufacture the samples.

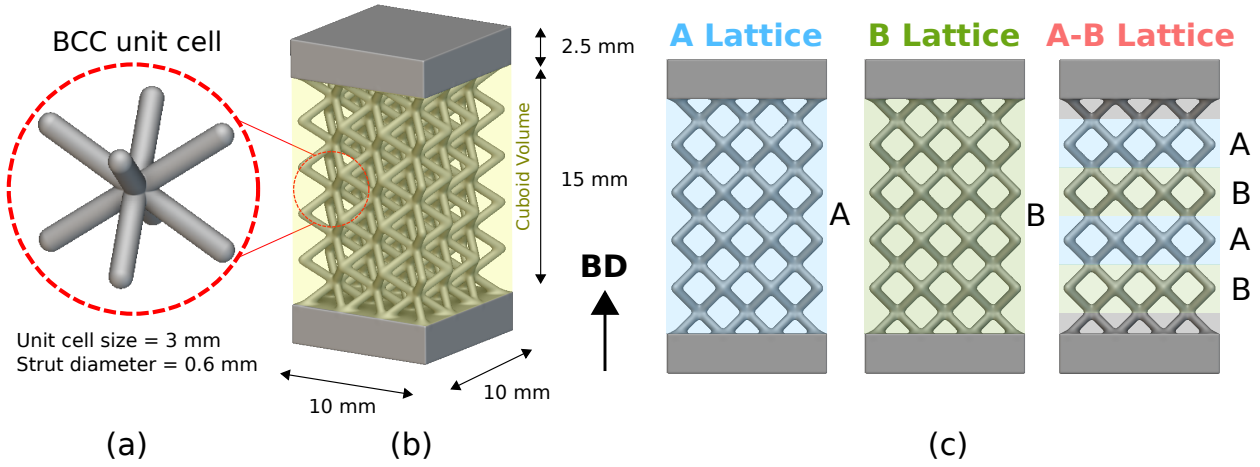

Figure 6.3: (a) BCC unit cell indicating the specific features selected for this work. (b) Measurements of the lattice structure designed for this work. (c) Lattice structures printed in this study. Blue and green indicate A and B set of process parameter employed respectively.

To study the effect of the processing parameters and its functionalised grading on the lattice structures, different sets of processing conditions were used, see Figure 6.3c. The first two lattice types (Lattice A and Lattice B), were manufactured using two different set of processing parameters (A and B) detailed in Table 6.1. These two sets of process parameters were carefully selected, based on their actuation response from a previous fundamental study of Garrido *et al.* [194] assuring a low porosity and differing actuation properties. Set A presents

a low VED which results in lower TTs and Set B presented a higher VED resulting in higher TTs [194]. The third lattice was manufactured with a graded pattern of processing conditions as indicated in Figure 6.3c, alternating regions manufactured using high VED and others with low VED. For all the three different lattices, an optimized set of process parameters was used for the lower and top caps and its connection with the lattice.

Parameter ID	**P (W)**	**v (mm/s)**	**h (µm)**	**VED (J/mm^3)**	**LED (J/mm)**
A	72	990	48	50	0.073
B	125	668	48	130	0.187

Table 6.1: LPBF processing parameters used in the manufacturing of NiTi lattice structures samples. VED was calculated as VED = P/(v · h · t) where P is the laser power, v is the scanning speed, h is the hatch spacing and t is the layer thickness. LED was calculated as LED = P/v.

6.2.2 Material characterization

Measurement of the solid fraction

To analyze the overall geometrical deviation and manufacturability of the different lattices, the solid fraction of each produced sample was studied. This was done by the measuring the weight of the lattice structure $W_{lattice}$ and divided by the theoretical bulk mass of the cuboid volume as:

$$RD(\%) = \frac{\frac{W_{lattice}}{\rho_{NiTi}}}{V_{cuboid}} \cdot 100 \tag{6.1}$$

where V_{cuboid} is the volume of the cuboid as indicated in Figure 6.3b and ρ_{NiTi} is the theoretical density of NiTi ($6.45 g/cm^3$). The weight of the lattice structure $W_{lattice}$ is calculated by subtracting the weight of the bulk top and bottom plate to the total weight of the manufactured lattice.

Analysis of the strut diameter distribution and cell pore size

To estimate the diameter of the struts and the cell pore size, images of the samples were captured using a Hitachi S-3400N Scanning Electron Microscope (SEM) with magnifications of 11x, 25x and 75x at a beam voltage of 15 kV, and high image contrast. These images were

used to estimate the statistical distribution of strut diameters and cell pore sizes for each lattice condition (A, B and A+B as in Figure 6.3 c) through image analysis.

Microstructural characterization

The metallographic preparation of the samples involved an initial grinding step using up to 1200-grit abrasive paper, followed by a polishing stage involving 9 µm and 3 µm diamond suspension. A final step with colloidal silica suspension was performed. The polished specimens were etched using a solution of H_2O (80%) + HNO_3 (15%) + HF (5%). The images of the samples were captured using a Hitachi S-3400N Scanning Electron Microscope (SEM) with magnification of 4000x and a beam voltage of 15 kV, and high image contrast.

6.2.3 Mechanical testing

Thermomechanical tests of the lattice samples were conducted in an universal mechanical testing machine equipped with a climate chamber. The thermomechanical tests performed in this study were actuation tests, specifically maintaining a given load while performing a thermal cycle to observe the entire austenite-martensite transformations of the lattice structure as indicated in Figure 6.4a. The thermal cycle starts by cooling the lattice from 440K to 300K and then heat it up again to 440K (a whole thermal cycle) to extract the direct and inverse TTs. To study the effect of the stress on the transformation, the same thermal cycle was performed under constant forces of 250, 500, 750, and 1250 N. The samples were heated and cooled at a rate of 10 K/min. Thermocouples were attached to the plate of the lattice to assure that real lattice temperatures were measured. The macroscopic strain of the samples was measured using Digital Imaging Correlation (DIC) [275]. From the combined analysis of strain and temperature data, the TTs along with the recoverable and plastic strain were extracted according to Figure 6.4b.

6.2.4 Computational approaches

To study the preferable transformation sites of the lattice structures, stress distribution analysis was performed on the printed geometries through computational finite element analysis (FEA). To capture the effect of manufacturability and geometrical deviations from the processing, the simulated lattice geometries were designed using the mean diameters obtained from experimental data. For the graded lattice that combines both sets of parameters

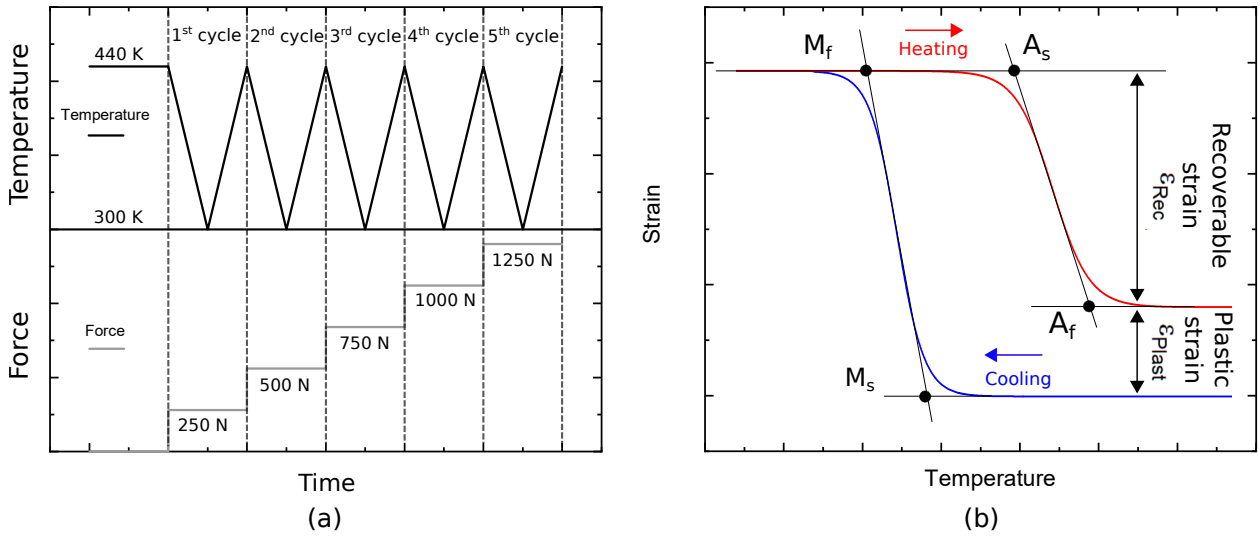

Figure 6.4: (a) Detail of the temperature and force evolution during the actuation tests in this study. (b) Exemplary diagram of the variables extracted from the temperature - strain data measured during the actuation tests.

designated as A-B, each row of unit cells was assigned a mean diameter corresponding to the respective manufacturing parameter (see Figure 6.3c). The lattice geometries under study were meshed using 3D linear tetrahedral elements (C3D4). ABAQUS 2023/Standard software package [248] was used to perform the simulations of the lattice geometries. In terms of boundary conditions, the displacement of the nodes positioned on the lower face of the sample was constrained in all directions through pinned conditions (Ux = Uy = Uz = 0). For nodes located on the upper surface, the displacement was restricted in the X and Y directions (Ux = Uy = 0), while a vertical compressive force on the Z axis was imposed equivalent to the 250, 500, 750, 1000 and 1250 N according to the experimental conditions detailed in the previous section. The constitutive behavior for the material was modeled as perfect linear elastic material model with an elastic modulus of 46 GPa extracted from previous studies [276] and the results of the the tensile test obtained in Chapter 4.

6.3 Results and Discussion

This section is structured as follows. First, the manufacturability of the lattices is analyzed and discussed depending on the processing parameters. Then, the microstructure of each lattice and the regions (for the case of graded lattices) is presented along with rationalization. Third, the results of the actuation tests are presented and discussed. Finally, the actuation properties obtained are analyzed.

6.3.1 Manufacturability analysis

Solid fraction

The solid fraction measured experimentally for each lattice geometry is presented in Figure 6.5. It can be observed that there are some deviations from the ideally designed solid fraction, which is greatly influenced by the set of process parameters used. The three lattice structures obtained solid fractions higher than desired. Lattice A presents the smallest deviation, while lattice B was the one with the largest deviation. This is reasonable as the parameter set B presents a higher VED than A, which can lead to over melting as the laser melts the solid. The reasons for this will be further discussed in the next sections. Furthermore, lattice structure A-B presents a solid fraction between lattices A and B, which is reasonable because it is a graded combination of both parameter sets.

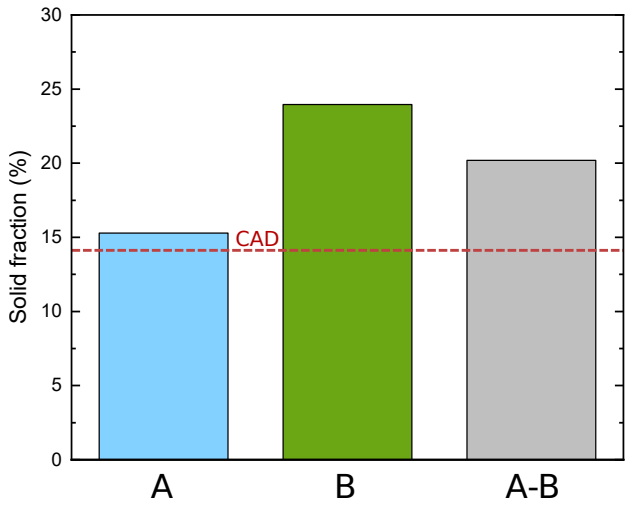

Figure 6.5: Experimentally mesaured solid fraction results of lattice structures fabricated using processing parameters A, B and graded A-B. Ideally designed solid fractions are also presented as black dotted line for comparison.

Surface analysis

Figure 6.6 shows different micrographs for each lattice structure obtained by SEM. As it can observed, the struts are well manufactured and continuous. No obvious structural flaws or processing defects were observed externally. All of the lattices surfaces exhibit rough surfaces. Looking at the magnified images it can be seen that this roughness is mostly produced by the powder particles adhered to the surface of the struts. The particles are preferentially adhered to

the lower part of the struts, which is associated with the accumulation of heat in these regions, as powder has a lower thermal conductivity than solid metal [277]. The heat accumulation in these regions, can lead to the partial melt of the powder particles next to the boundary line [278], and sticking the loose powder to the solid material during manufacturing [279]. There are different approaches to reduce the surface roughness associated to this phenomenon, like sand-blasting after manufacturing or off-setting the laser path before manufacturing [277, 280]. The excess of solid fraction observed in Figure 6.5 is probably partially caused by these powder particles partially melted to the lattice surface. Another phenomenon observed on the upper surfaces of some struts is the appearance of corrugations. These are inherent to the LPBF manufacturing process as a result of the layer-by-layer production of the material. The presence of surface roughness associated with this manufacturing process is one of the aquiless hails of AM. This can undermine the fatigue life, ductility and/or strength of the manufactured metal [281]. The roughness associated with the corrugations can especially affect the fatigue performance of the lattice, acting as stress concentration points, as they are inherent to the material in contrast to the cited adhered powder particles. Corrugations can be minimized by increasing the beam power or decreasing the layer thickness, although the last increases the fabrication time and presents limitations [282]. Finally, for all samples, no broken struts or obvious defects were observed.

Strut diameter and cell pore size

To statistical analyze the geometrical deviation of the manufactured lattices, the distribution of strut diameter and cell pore sizes has been measured. The average strut diameters are shown in Figure 6.7a along with their standard deviations. All of the lattice structures have strut diameters that are larger than the ideal designed ones. Lattice A is the one with the average strut diameter closes to the designed one, followed by lattice B. A similar trend can be observed for the case of the cell pore size, presented in Figure 6.7b. The measured cell pore sizes are always below than the ideal designed ones for all lattice structures. The results of the diameters and pore sizes of the lattice A+B were classified based on the used process parameters, which showed similar results as in their corresponding monoparameter lattices. Both observations, the higher strut diameter and the lower pore size compared to those designed, can be explained by two connected phenomena. First, the powder observed in the micrograph of Figure 6.5 partially melted on the surface of the lattice increases its strut diameter and reduce the effective pore size. Second, higher energy inputs can lead to spread the thermal footprint of the laser to larger regions, leading to over-melting beyond the contour region, increasing the solid area of the lattice. The thermal footprint of the laser

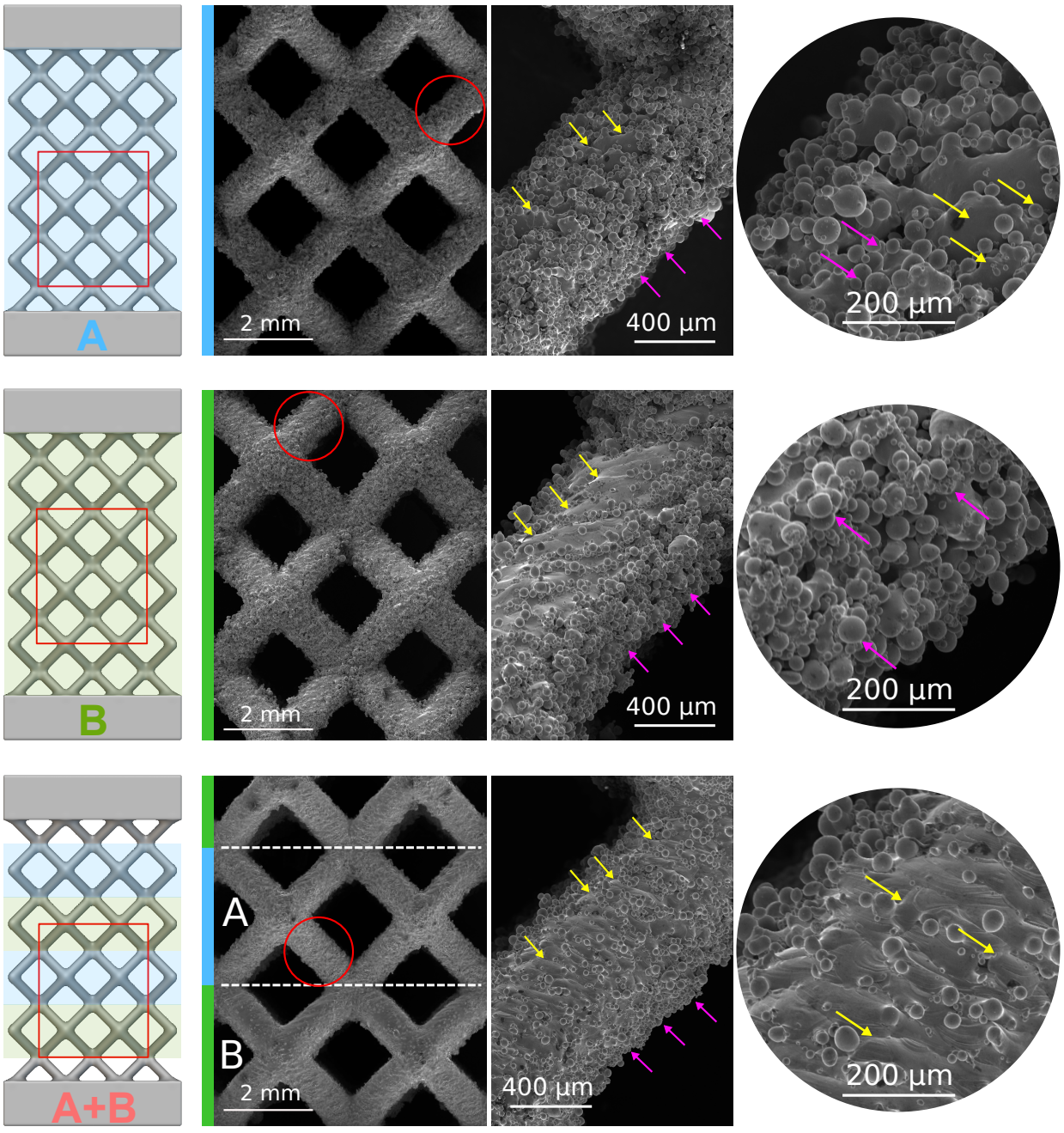

Figure 6.6: SEM micrographs of the different lattice structures. Powder particles and layer corrugations are marked in the magnified micrographs with pink and yellow arrows respectively.

track is directly related to the linear energy density (LED). The set of process parameters A presents a low LED, while set B presents a higher LED, see Table 6.1. Wider and deeper tracks are formed when a higher LED is utilized [249]. This can explain the higher strut diameter observed for the set B (see Table 6.1).

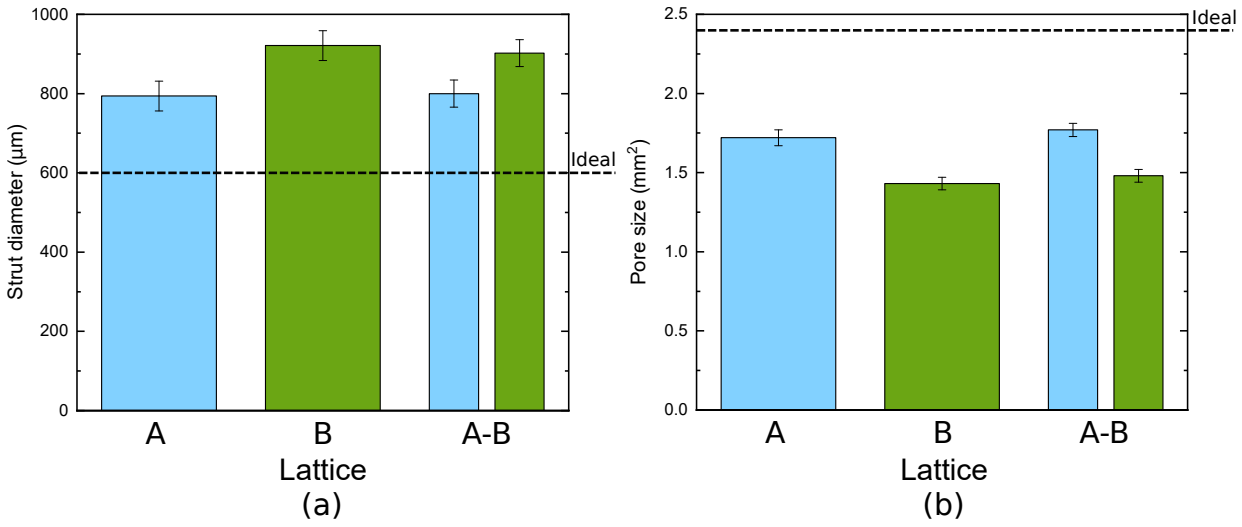

Figure 6.7: (a) Diameter and (b) pore size distributions of the printed lattice structures. The target design is pointed out as a black dotted line.

The presented results show that the process parameters used to fabricate the lattice structures critically affect the final produced geometry and its deviations from the ideal design. Lattice design is the same for the different sets of processing parameters used, which means that the slicing done before the manufacturing process is unchanged. With the same scan tracks, the wider and deeper melt pools produced by process parameters B produce a lower printing accuracy as a result of greater amount of melted material involved during the LPBF process. The geometrical deviation is also influenced by the orientation and diameter of the struts [277].

6.3.2 Microstructural analysis

The microstructure developed from the manufacturing process has been analyzed through SEM. Figure 6.8 shows the SEM micrographs obtained for each of the lattices and regions. Critical differences in these microstructures can be observed as a function of the process parameters used for manufacturing the material. For the case of high VED parameter set (Lattice B), black spot precipitates can be identified throughout the microstructure. Previous studies have identified these precipitates as Ti_2Ni. In contrast, the micrographs of samples

manufactured with low VED parameters (Lattice A) do not show these precipitates and instead, only show martensite plates with differing gray scales. Similar results are obtained for the case of the graded lattice A+B, in which regions manufactured with high VED (B) are populated by Ti_2Ni precipitates in similar arrangements to the single parameter lattices and the regions manufactured with low VED (A) present marks of martensite plates. In a previous study (see Chapter 4), the presence of Ti_2Ni precipitates is linked to the higher evaporation of Ni occurring at higher VED, due to the lower evaporation temperature of Ni when compared to Ti. Having a Ti-rich matrix leads to over-saturation of this element and precipitation of the Ti_2Ni precipitates. These precipitates have been found to play an important role in the transformation behavior of this type of alloy [194, 283, 209], by controlling the nucleation and propagation of the austenite and martensite phases during phase transformation. Therefore, the control of this precipitation through LPBF can modulate the thermomechanical behavior of the alloy. This will be linked to the mechanical behavior of the different lattices in the following sections.

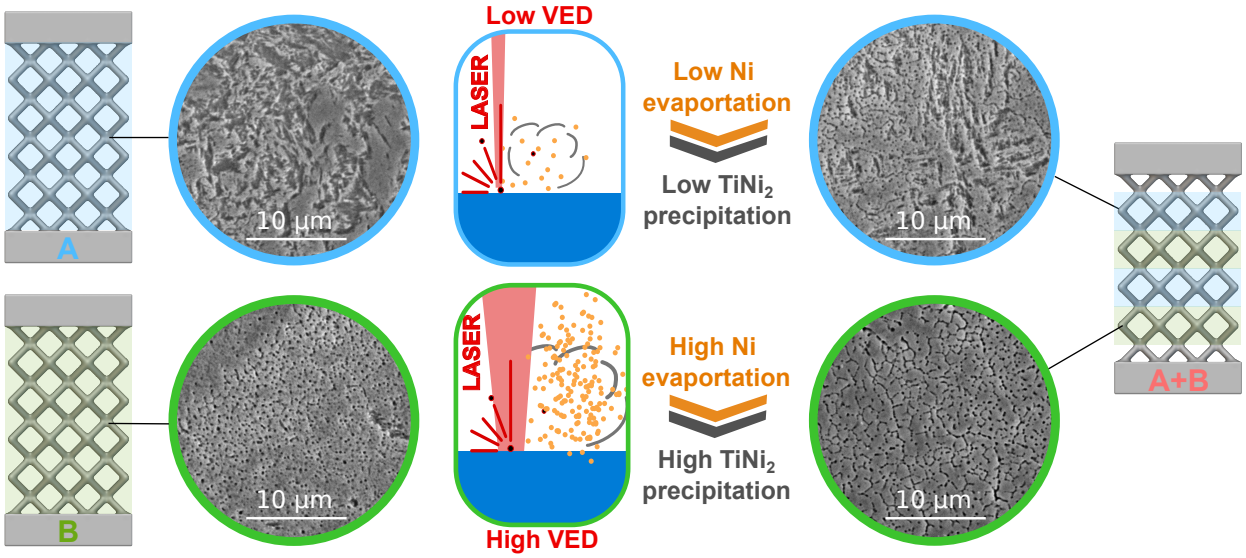

Figure 6.8: Microstructural analysis of the lattice structures of this work.

6.3.3 Thermomechanical behaviour

Figures 6.9a-e illustrate the strain-temperature curves of the actuation tests of the manufactured lattice structures under a compressive force of 250, 500, 750, 1000 and 1250 N respectively. It is important to note that we refer here to effective strain of the lattice, as the strain arising from dividing the difference in displacement from the top and bottom plate divided by the total height of the lattice. Each graph shows this effective strain response of

each of the lattice configurations (A, B, and A-B) as a function of temperature for a given load. It can be observed that the temperature-deformation cycle follows a similar shape for all the applied forces and lattice configurations. First, the strain suffers a negative deformation during the initial cooling event (1) produced by the austenite ⇒ martensite transformation. Then, in the heating cycle (2), the previously transformation induced deformation is partially recovered due to the martensite → austenite transformation. The difference between the starting point and end point of the cycle is the plastic residual strain. This strain will be further analyzed in the actuation response section. It is interesting that across all force levels, lattices A and B display distinct thermomechanical behavior, with the lattice A-B curves generally falling between the other two. As the compressive load increases, the magnitude of the strain continuously increases for all lattice structures, indicating greater deformation under higher forces. In addition, the enclosed area inside the curves increases with higher loads.

Although the results demonstrate that the effective strain-temperature relationship of the lattice structures is strongly dependent on the applied compressive force, a deeper analysis is required to find material dependencies. For the case of bulk testing, the stress-strain curves directly relate the behavior of the underlying material as the macroscopic stress and strain coincide with the microscopic stress and strain, in the absence of localized deformation, and if the local stress and strain fields produced by the microstructure are omitted. However, for the case of lattice and porous structures, the macroscopic stress and strain do not coincide with the local stress and strain state of the material. The stress state in a lattice structure is far from being uniaxial, and it changes with geometry arising from manufacturing deviation and defects. As discussed previously, the processing parameters impact the diameter of the printed struts (see Figure 6.7a), obtaining larger diameters using the process parameters B. This problematic becomes exacerbated by the well-known strong dependency of the transformation on the local stress experienced by the material [194, 284, 285]. This makes necessary to perform a more complex analysis if the relations between processing parameters and resulting thermomechanical behavior of the lattices want to be fully understood.

To this end, the whole lattice with its real dimensions has been simulated with the real load applied in the experiment to extract the local stress fields of the material. The exemplary stress fields for the case of 1250N are presented in Figure 6.10. It can be observed that the stress field is far from being uniform neither uniaxial as in a bulk tensile samples. To compare the phase transformation and actuation behavior of lattice structures with the results of bulk material, a measurement of the effective stress in the lattice needs to be addressed. This effective stress can be calculated from the volumetric average of the Von Mises stress field in

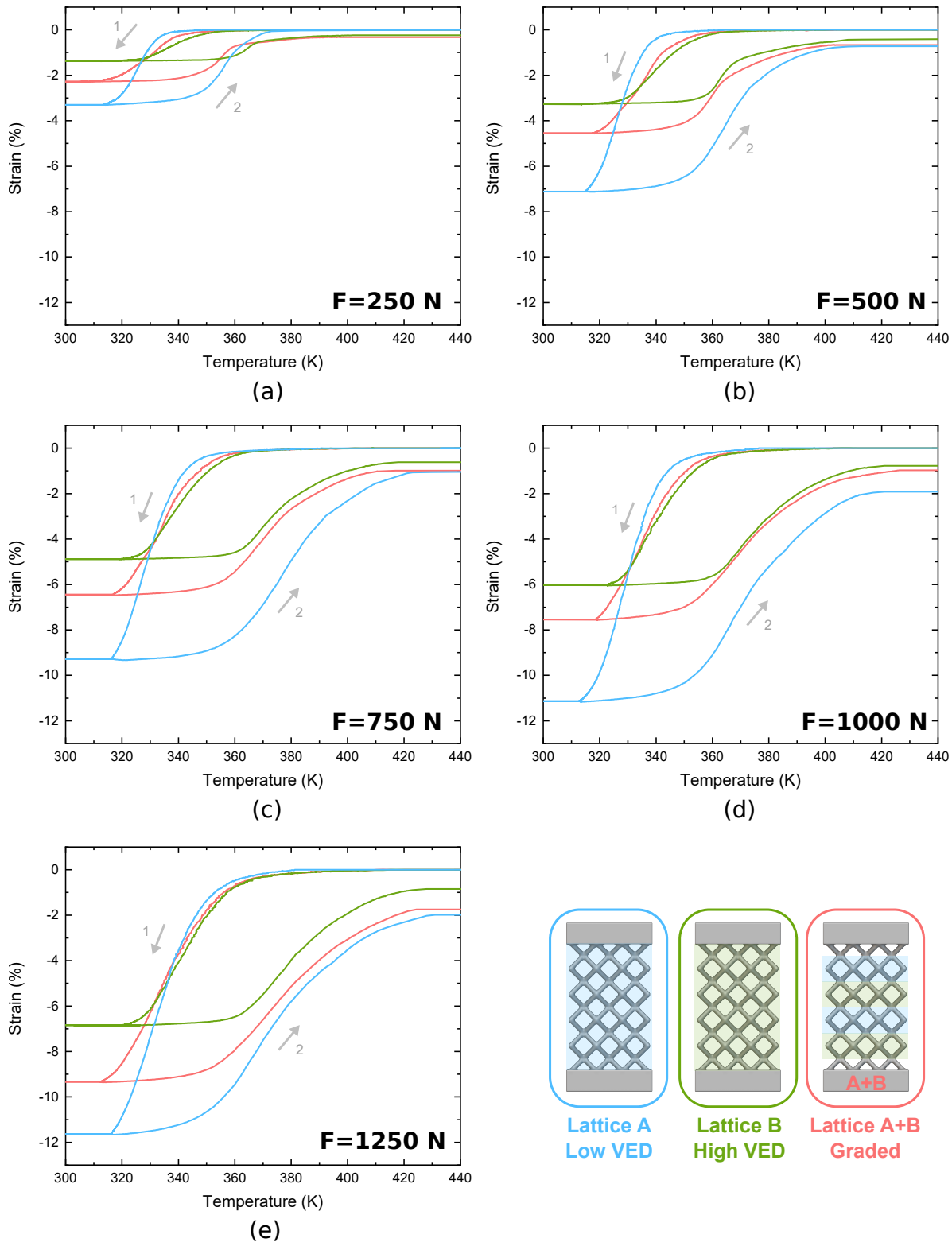

Figure 6.9: Actuation behavior under compression at a force of: (a) 250 N, (b) 500 N, (c) 750 N, (d) 1000 N and (e) 1250 N. Blue, green and red represent the lattice structures fabricated with each processing configuration A, B and A-B, respectively.

the simulated lattice:

$$\overline{\sigma} = \frac{1}{V}\int_V \sigma^M dV = \frac{1}{V}\sum_{elements} V_i \sigma_i^M \tag{6.2}$$

where V_i is the volume of the element i, σ_i^M is the Von Mises stress in element i and V is the total volume of the analyzed area. The resulting average Von Mises for each lattice structure is presented in Figure 6.10. The results indicate that as the diameter of the strut increases (lattices A to B), the average stress within the lattice structure decreases. Consequently, the struts printed in lattice A, which present a lower strut diameter when printed, experience higher stress levels for the same compressive load. These average stress values $\overline{\sigma}$ will be utilized in the subsequent sections to normalize stress, facilitating a comparative analysis of thermomechanical features.

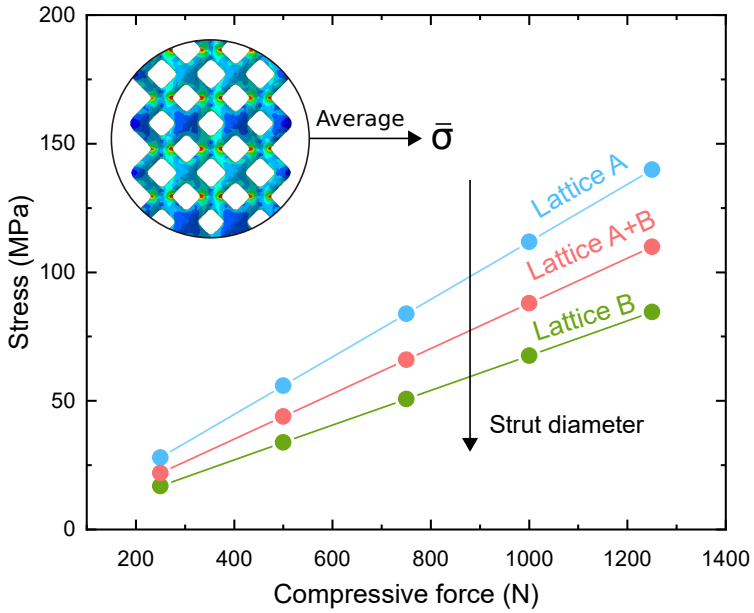

Figure 6.10: Average Von Mises stress of each lattice structure experienced in the FEA simulations under a constant load of 250, 500, 750, 1000 and 1250 N.

6.3.4 Phase transformation

To contextualize the effect previously discussed, the martensite start transformation temperature (M_s) is shown in Figure 6.11a for all lattice structures as a function of the average lattice stress, $\overline{\sigma}$, previously calculated. Despite the fact that the struts are subjected to different stress levels, once the load is normalized using the average Von Mises stress, the phase transformation behavior differs across the lattice structures, which points out the real effect of the process parameters on the phase transformation through microstructure modification.

To compare with the results of the bulk material, M_s extracted from the previous study (see Chapter 4) using the same processing parameters is displayed.

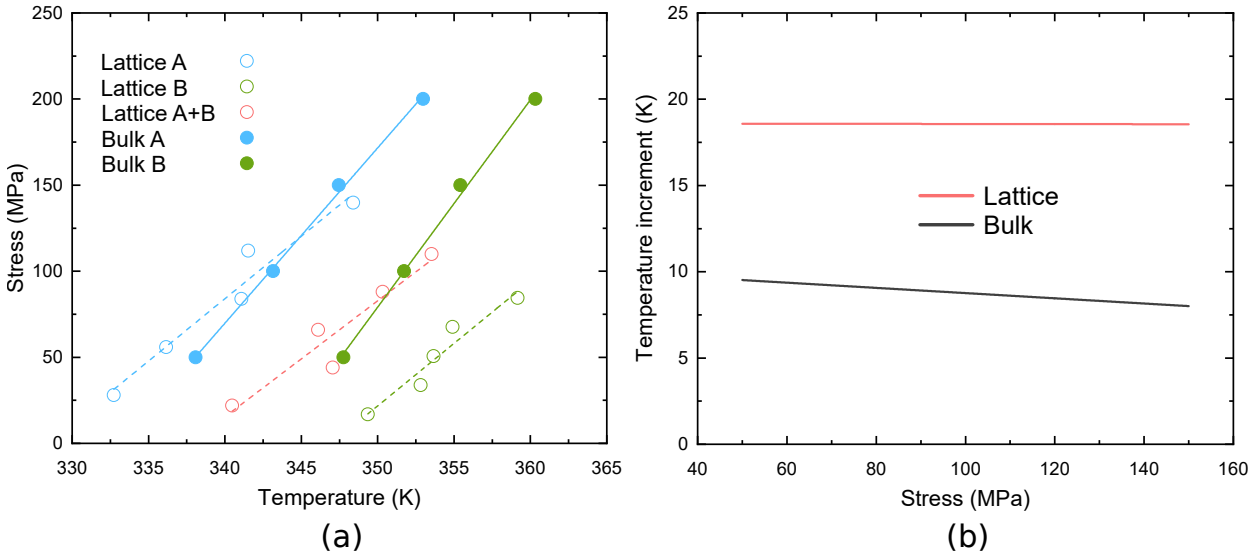

Figure 6.11: (a) Martensite start temperature (M_s) for each lattice structure and the average Von Mises stress from FEA for each lattice structure. The results of the tensile samples manufactured using process parameters A and B are also displayed (see Chapter 4); (b) Difference between the maximum and the minimum M_s values obtained for each stress level for lattices and bulk material.

For the case of the lattice M_s temperatures (unfilled points) a consistent trend is observed for all the stresses studied: lattice A presents the lowest M_s and lattice B the highest M_s, M_s of the lattice A-B lying between them. The difference between lattices A and B ranges $\sim$ 15-20K (see Figure 6.11b). This difference is important because it sets the capability of tailoring the response of the lattice structure by modification of the processing parameters. A similar effect occurs in bulk samples, where the one manufactured using process parameter B obtained higher M_s than the one printed using process parameter A. In this case, the difference in M_s between the higher energy parameters (B) and the low energy parameters (A) is $\sim$5-10K (see Figure 6.11b). This shows the catalytic effect of the lattice geometry in modifying the transformation temperature of the cellular structure. Based on these results, M_s of the lattice structures are highly influenced by the processing parameters employed during fabrication. This is in agreement with the previous microstructural analysis shown in Section 6.3.2. As the VED input of the laser increases from A to B conditions, the Ni evaporation increases, leading to a lower Ni/Ti ratio, which was correlated in Figure 6.8 with a higher concentration of Ti_2Ni precipitates. This reduction in the Ni/Ti ratio produces an increase in the TTs of the alloy as previously indicated in other studies [194, 286, 195].

Furthermore, an interesting observation from the figure is the change in the stress dependence factor of the transformation temperature M_s (represented by the slope of the lines) between lattice structures and the bulk material for the same process parameters. The three lattice configurations (A, B and A+B) exhibit a lower stress dependence than the bulk material. This suggests that the way in which these structures are subjected to loading influences their transformation behavior. Reedlunn *et al.* [287] studied in a detailed way the influence of the different loading conditions in SMAs. They tested the same alloy under compression, tension, and bending, discovering different responses. They found that the way the transformation front evolves in the material differs between tension, compression and bending loading. Transformation fronts were more uniform for the case of compression except in the buckling areas. However, for the case of the bending, the strain fields of the sample contained localized strain just on the tensile side, indicating that some parts located at the compression region did not undergo full transformation at the end of the load application. This leads to variations in the transformation behavior depending on the loading condition of the material. This might be the reason behind the higher stress dependency observed in the bulk material compared to the lattice material. In tensile samples, the applied stress is uniformly distributed across the entire geometry, leading to a more consistent transformation behavior. In contrast, lattice structures experience a combination of bending and compression loads, resulting in non-uniform stress distribution as shown previously in Figure 6.10. Certain regions of the beams are subjected to lower stress levels, causing different phase transformation across the geometry. This effect might reduce the overall influence of stress on phase transformation, thereby reducing the observed slope.

To further confirm this point, the local transformation behavior will be analyzed using the DIC data obtained from the test. Figure 6.12 represents 2D strain maps of the lattice structures during the forward transformation (austenite $\Rightarrow$ martensite) when they were subjected to a compressive load of 1250 N. The frames shown correspond to 0, 25, 50, 75 and 100% of the half cycle (cooling event). It can be observed that, as the temperature decreases, the forward transformation does not begin at the same time at all points of the structures. Transformation strain begins in the lateral parts of certain nodes. Subsequently, it propagates to the beam regions and finally extends throughout the entirety of each beam. It is interesting to note that based on the measured strains, the nodes of the lattice structures did not undergo a phase transformation. In addition, for the case of lattice A-B, the unit cells manufactured using process parameter set B do not show an appreciable change in the temperature setting the start for the local transformation temperature when compared to those manufactured with parameter A as happened in the mono-parameter lattice structures A and B (see Figure

6.11a). This is an interrelation effect between the unit cells printed with A and B parameter set in the A+B lattice which is not present for the case of monoparameter lattices.

To further elucidate this effect, the local stress state of each type of lattice is presented in Figure 6.13 for a compressive force applied of 1250 N. In all lattice structures it can be observed how the stress concentration was in the side region of the internal nodes that coincide with the same place where the forward transformation starts in Figure 6.12. So, as the temperature decreases, the areas with the highest stress concentration undergo the initial phase transformation. As these areas transform, new local stresses appear in the rest of the beams which act as a driving force to continue the forward transformation on these areas. In contrast, Figure 6.13 also shows how the nodes are subjected to low stress concentrations in all structures, and this is the reason why they do not undergo phase transformation. The simulation results represent an idealized structure, without the roughness and corrugations observed in Figure 6.6. However, the highest stress concentrations are located on the sides of the internal nodes. Furthermore, Figure 6.13 presents the M_s transformation temperature distribution for each lattice structure, based on data extracted from Figure 6.11a. It can be observed that in all three lattice structures, the highest M_s values are located on the sides of the internal nodes, indicating that these regions will undergo the initial phase transformation during cooling. Lattice A exhibits lower M_s regions compared to Lattice B, which aligns with the results of the phase transformation. Although Lattice A exhibits higher stress compared to Lattice B, the effect of process parameters on the M_s temperature causes Lattice B to show a higher M_s. Consequently, phase transformation occurs earlier in Lattice B than in Lattice A. A similar combined effect is observed in Lattice A+B, where unit cells fabricated using process parameter B display higher M_s values, suggesting that these regions will undergo phase transformation earlier during cooling compared to those manufactured using the parameter set A. In real experiments, the real morphology introduces variations in stress concentration, leading to a phase transformation initiation that differs exactly from the simulation predictions.

6.3.5 Recoverable strain

As indicated before, one of the main objectives of this study is to achieve considerable changes in the actuation response of the lattice structures by local modulation of the microstructure through the LPBF parameters. The main variables defining the actuation response are the recoverable strain and plastic strain. The recoverable strain is displayed in Figure 6.14 for each given average Von Mises stress $\overline{\sigma}$. For direct comparison and scientific discussion, the

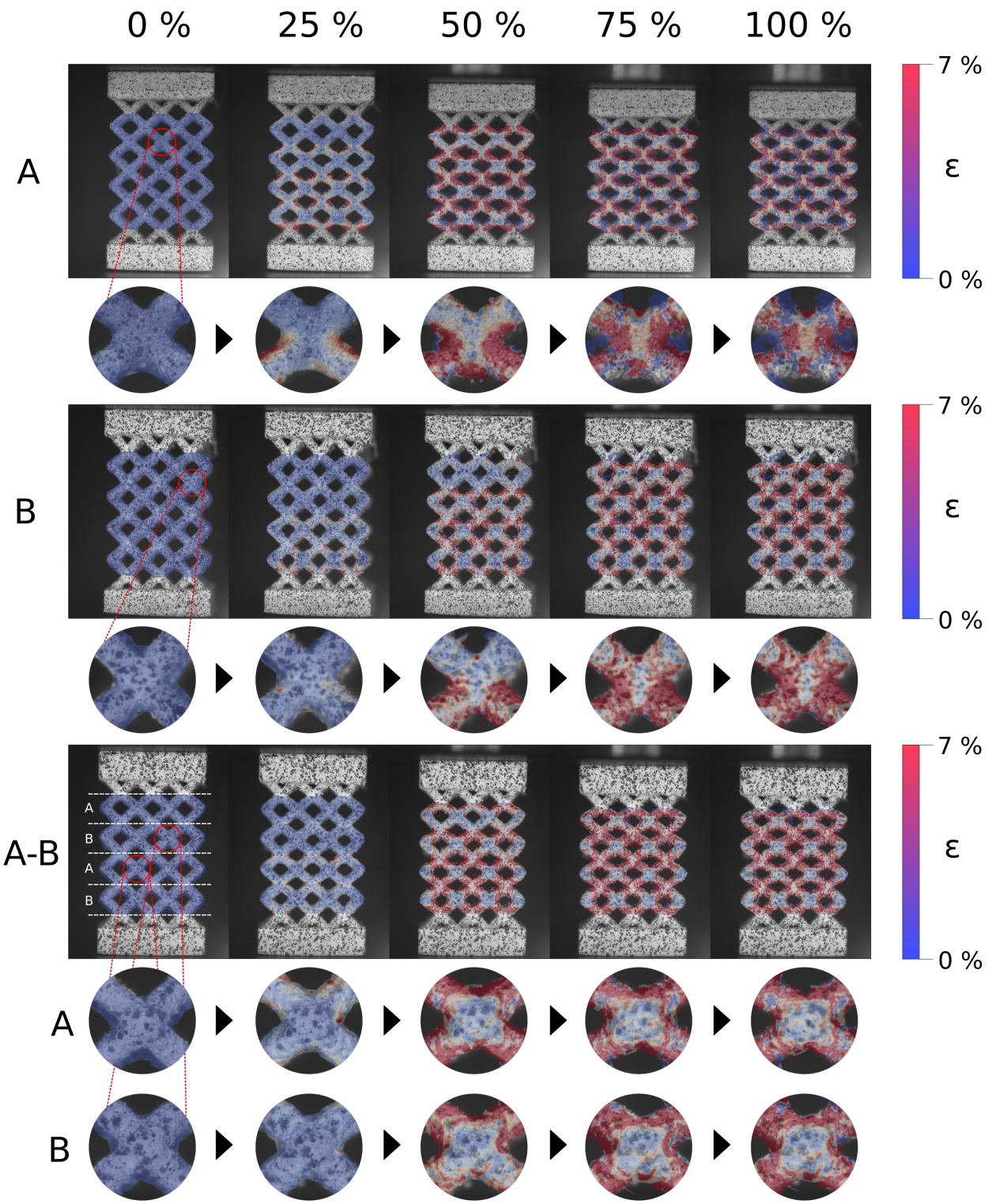

Figure 6.12: Deformation color map of the lattices A,B and A-B in the thermomechanical cycle subjected to a compressive load of 1250 N. The frames shown correspond to 0, 25, 50, 75 and 100% of the forward transformation.

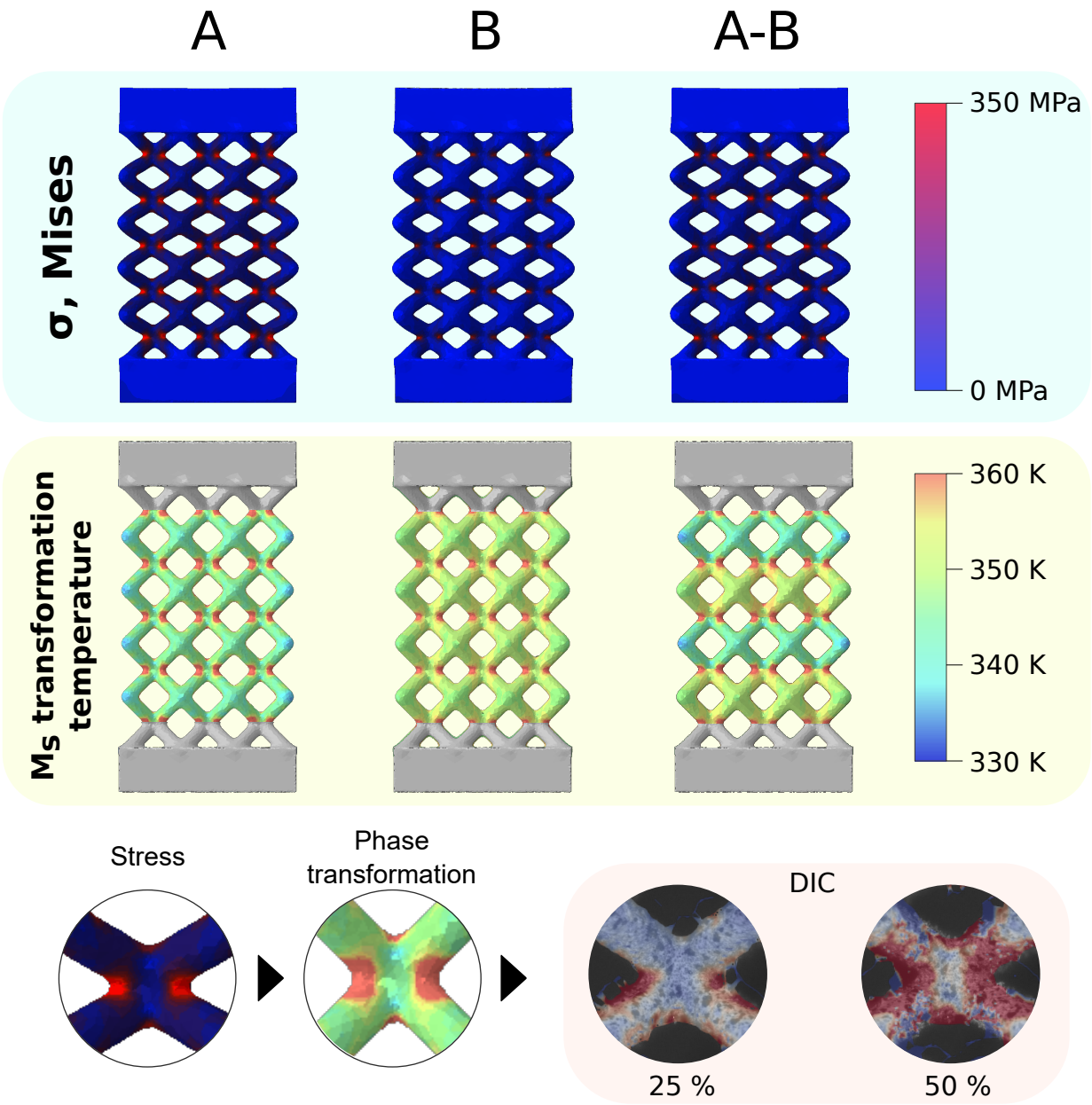

Figure 6.13: Von Mises stress and martensite start temperature (M_s) after applied a compressive force of 1250 N in each lattice structure.

recoverable strains of the bulk material produced with the same parameter sets A and B are plotted as filled data points, extracted from the previous work on the same alloy powder (see Chapter 4). The stress dependency in the recoverable strain of the lattice structures is clear. A higher stress is translated into a higher recoverable strain of the lattice structures. The slope in the strain recovery of Lattice A appears to indicate the saturation of the recoverable strain at higher stresses. This tendency is in agreement with the data observed for the bulk material. Lattice A displays the highest recoverable strain for all stresses, followed by lattice A-B and finally lattice B. The lower recoverable strains of lattice B can be caused by the presence of Ti_2Ni precipitates in the microstructure produced by parameter set B, as previously indicated by previous studies [194, 225]. The coherent non-transforming precipitates affect the total transforming volume, producing lower recoverable strains [219].

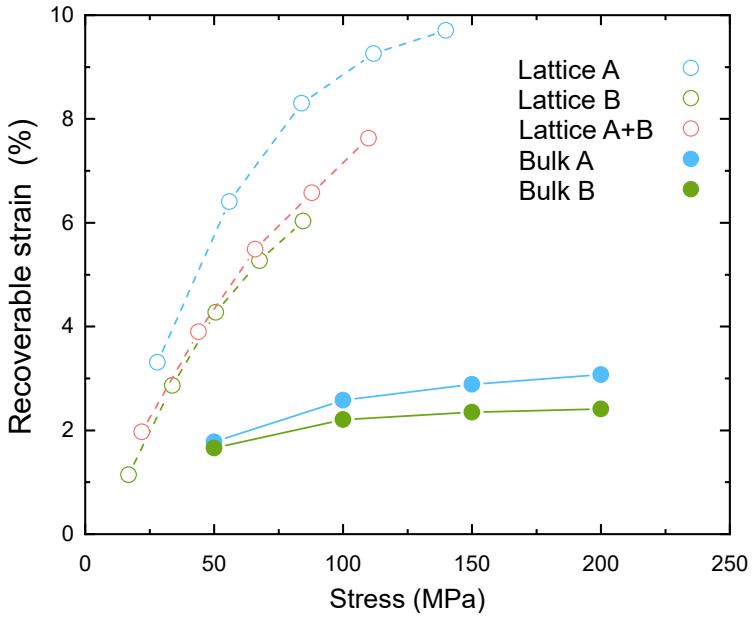

Figure 6.14: Recoverable strain for each lattice structure under the average Von Mises stress of the lattice structure. The results of the bulk material using process parameters A and B are also displayed (see Chapter 4).

It is interesting to note that there are important differences in recoverable strains between cellular behavior and bulk material. For all cases, lattice structures obtained between 2 and 3 times the values of recoverable strains of the tensile samples. Three different points have been identified as potential precursors of this: (1) the multiplicative effect of cell structure in transferring microstrains to macrostrain, (2) the effect of the complex stress conditions on the phase transformation in SMA and (3) the orientation dependent microstructural effect.

The most important one is the multiplicative effect of open cell structures in transforming

small microstrains into a large macroscopic strain of the whole structure. Figure 6.15 shows this phenomenon. In a uniaxial loaded bulk structure, either in tension or compression, the local transformation strain is transformed directly in a macroscopic strain of the same magnitude. But for the case of a non-uniaxial loaded beam, small microstrains can be translated into large macrostrains: e.g., a beam of length $L = 5mm$ undergoing a local 0.5% transformation at the surface of the beam can lead to displacements at the tip of the beam of up to 4% of the total length. This phenomenon has been utilized historically to develop complex geometrical arrangement combining multiple elements in the fabrication of smart SMA actuators [288, 289, 290]. But for the case of the cellular structures, this effect is inherently heritage by the own nature of the cellular structure geometry (a compound of multiaxial beam structure). The results presented here confirm this powerful capability enabled by the AM of lattice structures to increase the actuation response of SMA materials. The second

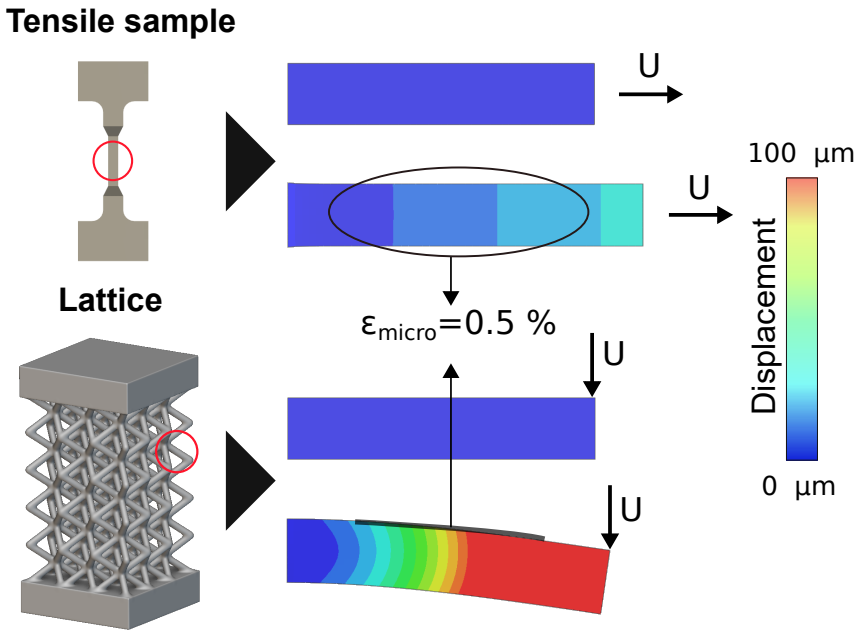

Figure 6.15: Multiplicative effect in transferring microstrains to macrostrains in cellular materials and its effect in the actuation behavior.

effect, as previously discussed, is the effect of the local stress state on the transformation behavior of the SMA. It is important to note that the local stress state is not the same for the case of the beams in the lattice structure and the bulk tensile sample. Tensile samples present a homogeneous uniaxial stress distribution, causing the appearance of an homogeneous transformation frontier [287]. On the other hand, lattice structures, as can be observed in Figure 6.13, present a more complex loading state. The macroscopic compression of the lattice translated into compression and bending loads in the beams oriented 54° from the building

direction. This produce heterogeneous non-uniaxial stress fields in the local material which differ strongly from the uniaxial homogeneous tensile stress state in bulk samples. This has an impact in the transformation which has been studied before in the literature [287, 291]. Bechle *et al.* and Reedlunn *et al.* observed the strain fields in bending samples contained localized strain on the tensile side, but no such localizations on the compression side of the tube. They observed that bending resulted in localized nucleation of martensite. Localization regions started as fine angled fingers that eventually coalesced into wedge regions distributed along the length of the tube [287, 291]. This is caused by the tension-compression asymmetry due to NiTi exhibit higher critical stress in compression than in tension [292]. This means that on the compressive side of the pseudoelastic bending tube, the material remains in the austenitic phase longer, limiting the strain. In addition, some studies found that compression samples experienced higher recoverable strains than in tension due to this asymmetric behavior [287, 292, 293]. The tension–compression asymmetry is generally attributed to the crystallographic asymmetry of the martensitic phase transformation [287].

The effect of the underlying microstructure. Although it has been confirmed similar results in the precipitation distribution between lattice and bulk material, the grain orientation should be affected by the orientation of the strut. Literature shows that the grain structure developed from the LPBF of NiTi alloys process follow the build direction [28, 195]. This is produced by austenite grains growing along the build direction with a [001] orientation, effect which is more pronounced when increasing the VED [249]. For the case of the tensile bulk samples in the previous work (see Chapter 4), the loading direction of the sample coincide with the building direction. However, for the case of the lattices in the current work, each of the beams in the BCC lattice are oriented 54° from the building orientation. This can lead to differences in grain distribution and texture which have been shown to significantly influence the thermomechanical properties of LPBF SMAs [28, 23, 38]. Nematollahi *et al.* [28] found the highest recoverable strain samples printed at 45º than other vertically printed samples due to the formation of [100] texture in their microstructure. This is in agreement with our results as the lattice materials with strut orientation (54°) closer to 45° than the tensile samples (0°) present a higher transformation strain.

Finally, for a more addimensional study of recovery strain in SMAs, the recovery rate R_R is usually employed. The recovery rate R_R is defined as the percentage of the total strain ε_T that is recovered (ε_R) ,so $R_R = \frac{\varepsilon_R}{\varepsilon_T}$. Figure 6.16 displays the percentage of recovery rate of each lattice structure at the different stress levels. As previously reported, the recovery rates for the bulk material extracted from the previous study (see Chapter 4) are shown for comparison. It can be observed that the recovery percentage remains constant independently

of the load in the lattice structures and it is ∼85-90% independently of the process parameter used to print. Bulk samples present slight higher recoverable rates (∼90-95%). These findings emphasize the capacity of the structures to withstand repetitive stress and effectively revert to their initial shape, making them well suited for applications that require reliable and recoverable mechanical responses.

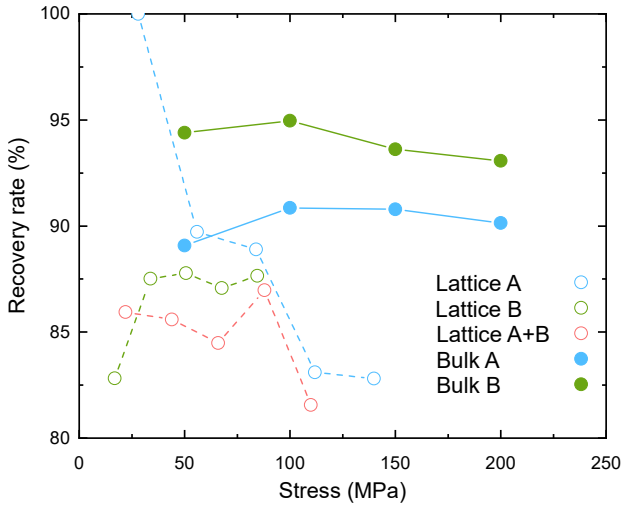

Figure 6.16: Recovery rate of the different lattice structures. The results of the tensile samples manufactured using process parameters A and B are also displayed (see Chapter 4).

6.3.6 Plastic strain

The other important parameter in the actuation response is the plastic strain. The plastic strain for each stress level is presented in Figure 6.17. Again, the results of bulk material samples from the previous study (see Chapter 4) are presented for the shake of comparison. Based on these results, all lattice structures demonstrate low and similar levels of plastic strain under compressive loads (all below 2.5%). In contrast to the recoverable strain, the difference between the lattice configurations is much less pronounced. However, when compared with the bulk material plastic strains the differences are noticeable. The plastic strain of the lattices are about 5-8 times the values of the plastic strain of the bulk materials. The possible causes behind this phenomenon are the same as previously mentioned for the case of recovery strain. First, in lattices, a small local plastic strain can be translated into higher macroscopic permanent deformation as previously explained for the strain recovery case (see Figure 6.15). This would explain the great difference between the plastic strain of the lattice structures and the plastic strain of the struts. Secondly, the orientation of the microstructure with respect to the loading direction can also influence the plastic strain observed. For the case of struts

in the lattice the building direction is oriented 54° with rested to the longitudinal axis of the strut while for the case of bulk material the longitudinal axis of the strut coincide with the build orientation. Based on previous studies [195, 191], considering that the underlying austenite grains grow following the [001] direction along the building direction, the highest Schmid factor of the tensile bars for BCC slip is 0 while for the case of a strut printed with 54° with respect to the building direction, the highest Schmid factor is around 0.41 [107]. This can result in more austenite slip in the lattice struts during the transformation and therefore more irrecoverable strain generated [224]. This of course is affected also by the stress conditions previously discussed and further analysis are necessary to fully understand this combined effect between microstructure and loading condition (e.g., development of orientation dependent models).

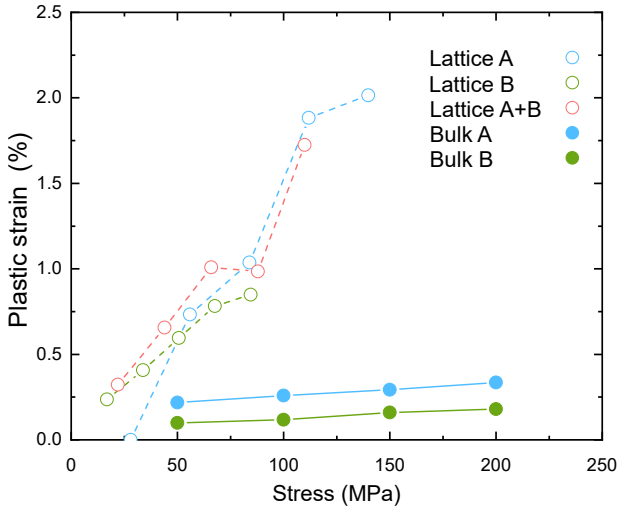

Figure 6.17: Plastic strain for each lattice structure as a function of the average Von Mises stress of the lattice structure. The results of the tensile samples manufactured using process parameters A and B are also displayed (see Chapter 4).

6.3.7 Design space for SMA lattice-based smart materials

To conclude, based on the obtained results and the discussion, two main effects control the thermomechanical behavior of the LPBF NiTi lattice structures: the geometry of the cell structure and the processing parameters used for each material point. The cell structure affects through the different loading scenarios and the way the local strains are translated to macroscopic strains. On the other hand, for the same cell configuration, the processing parameters influence the transformation stresses and temperatures through microstructural modulation. On the basis of these results, the synergy of combining latticing strategies

with processing modulation with the aim of modifying the thermomechanical behaviour of the SMA is clear. In Figure 6.18 the observed modulation effectiveness for each of the two design variables are presented for both the recoverable strains and the M_s transformation temperature. It can be observed the effect of the processing parameters on the modulation of the recovery strain is lower than the effect of latticing the material. On other hand, in the Ms temperature the effect of the processing parameters produce higher modulation of the phase transformation than the effect of latticing in the material. In both cases, the synergetic combination of LPBF modulation and latticing design present the highest design space for tailoring the thermomechanical behavior.

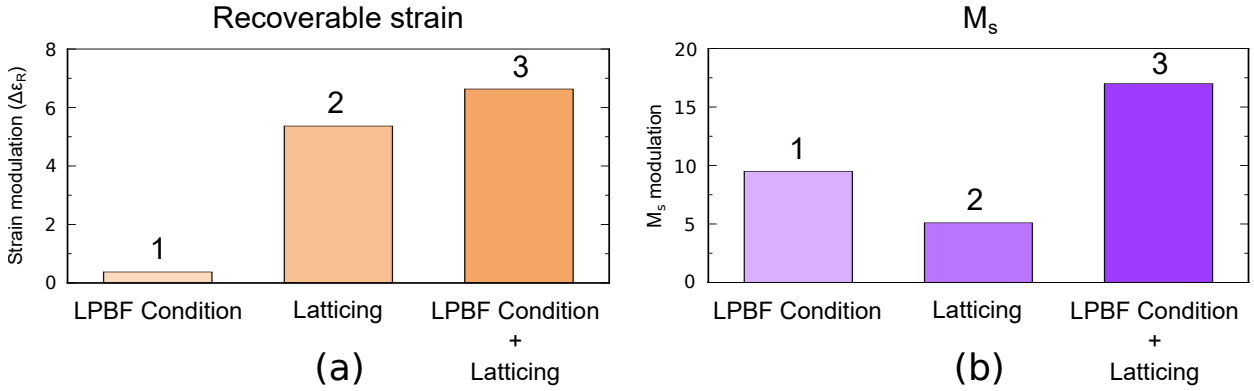

Figure 6.18: Effectiveness of the latticing and processing modulation in the design of the thermomechanical behavior of SMA cellular structures: (a) Recovery strain and (b) M_s transformation temperature.

To further elucidate the effectiveness of combining latticing modulation and processing modulation, the recoverable strains and solid fractions achieved in this work are compared with other studies in the literature using similar SMAs in Figure 6.19. The combination of high strain recovery with lightweight cellular structures presents interesting opportunities for actuator applications requiring low weight such as aerospace sector. Zhaorui *et al.* [294] designed lattice structures using BCC and octet unit cells with solid fractions of 50% and achieved recoverable strains of approximately ∼3%. Alberti Bifi *et al.* [149] developed lattice structures using a tetragonal diamond geometry with a solid fraction of ∼22%, reaching recoverable strains close to ∼ 4.5%. Andani *et al.* [29] fabricated three lattice structures using simple cubic unit cell obtaining solid fractions from ∼40-70% and recoverable strains of ∼5%. Dohyung *et al.* [295] produced a BCC lattice structure with the lowest solid fraction achieved at the moment (≤10%). Recoverable strain of ∼4% were reached. Lu *et al.* [296] manufactured three lattice scaffolds. The three structures were designed using pore sizes of 900, 835, and 618 µm. The unit cell changed between cellular structures to achieve solid fractions of ∼33%. Different recoverable behavior was found between ∼4-5.5%. Chen *et al.*

[297] employed topology optimization to design lattice structures with varying solid fractions across the rows of the unit cells, resulting in a global solid fraction of 30% and recoverable strains between ∼0.5-3.5%. Saedi *et al.* [25] printed three lattice structure with solid fractios between ∼40-70%. They observed that as the solid fraction of the structures was higher, the recoverable strain achieve increases (∼-2.5-3.5%). Ravari *et al.* [298] manufactured BCC and BCC-Z lattice structures achieving solid fractions of 31% for all samples and recoverable strains ranging 1.5-2.3%. Lingqi Sun *et al.* [299] designed surface lattice structures based on triply periodic minimal surfaces (TPMS) using diamond, gyroid, and primitive unit cells, achieving high solid fractions near ∼90% and recoverable strains between ∼5–9%. Xin Liu *et al.* [300] designed three lattice structures using topology optimization without a specific unit cell, obtaining solid fractions between ∼35–45% and recoverable strains ranging ∼1–3%.Yang *et al.* [148] designed a NiTi gyroid TPMS structure a solid fraction of 20% and unit cell size of 3 mm achieving recoverable strains of ∼5%.

In the present work, the three lattice structures with a BCC unit cell were designed and printed using different parameters, achieving solid fractions between 15–25% and strain recovery values ranging 6–10%. Based on the results in Figure 6.19, to the known of the authors, the structures designed in this work exhibit recoverable strains exceeding the ones previously reported NiTi lattice structures. These results paves set a first stone for a novel approach in the design of smart ad-hoc shape memory cellular structures, combining the synergetic effect of latticing structures and LPBF local modulation to design cellular structures with tailored thermomechanical properties.

6.4 Conclusions

In the present work, we have combined LPBF processing modulation with latticing strategies in a NiTi SMA to study a novel approach of designing smart meta-structures with tailored thermechanical response. The manufacturing accuracy, microstructure, phase transformation, and thermomechanical behavior were carefully studied for each geometry and processing regime. The following conclusions can be drawn:

1. Three NiTi BCC structures were successfully fabricated by LPBF using a different configuration of process parameters. Two lattices were printed with homogeneous parameter sets (A - low VED and B - high VED), and one lattice was printed with graded processing conditions (A-B-A-B).

2. The process parameters were observed to have a strong influence on the final geometries.

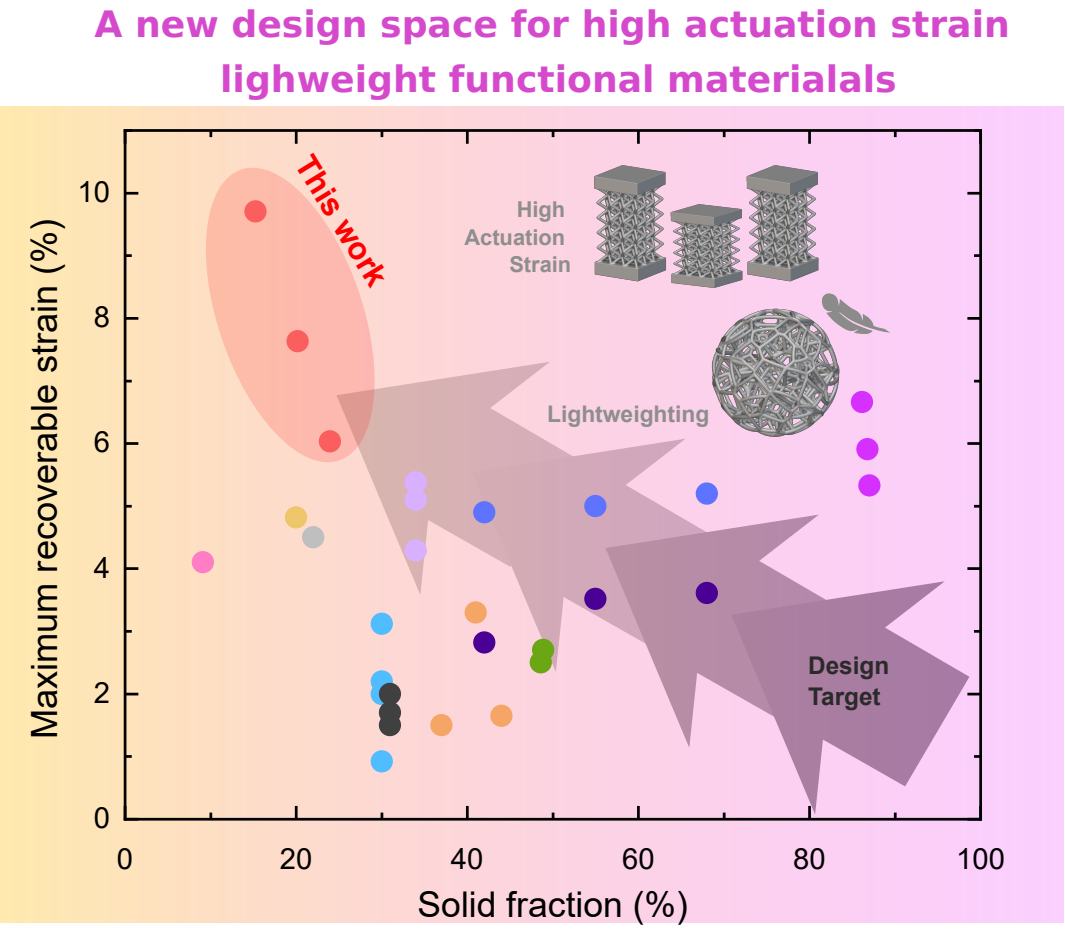

Figure 6.19: Maximum recovery strain-solid fraction diagrams comparing the lattice structures studied with the ones of other works: [294, 149, 29, 295, 296, 297, 25, 298, 299, 300, 148]

High VED parameters generate larger melt pools, leading to reduced printing accuracy, increased strut diameters, smaller pore sizes, and higher solid fraction. In contrast, lower VED parameters produce the opposite effect.

3. The lattices have been tested under compression to extract their actuation response under thermal cycling. The martensite start temperature (M_s) varies across the different lattices produced by different processing parameters, highlighting the influence of processing parameters on phase transformation through microstructural modifications. This has been linked with the reduced presence of Ti_2Ni precipitates and the highest Ni content when low VED was used due to Ni evaporation produced at higher VED. The use of latticing catalyse the change in the M_s by the change of processing parameters going from a change of 5K for to 15-20K when using latticing strategies. In addition, the lattice structures exhibit a lower stress dependence of M_s compared to the bulk material. This has been rationalized by the effect of non-uniform stress distributions and localized transformation behavior.

4. In terms of recovery strain, strain values ranging from 6% to 10% were obtained for the lattices under study compared to less than 2% for their bulk counterparts. This large difference has been rationalized mainly by the effectiveness of latticing in converting small transformation strains at the microscale level to large actuation strains at the macroscopic scale. Changes between different processing parameters were also observed, achieving higher recoverable strain when low VED parameters were used.

5. The effectiveness of combining both LPBF modulation and latticing strategies have been proved. The achieved modulation capability in the recovery strain and M_s by using both latticing strategies and LPBF modulation reach 2.5% change and 20K change, respectively. This is 2 and 4 times higher than what was previously achieved by just LPBF modulation.

6. The lattice structures designed in this study achieved maximum recoverable strain values ranging from 6% to 10%, being superior to those reported previously in the literature to the known of the authors. In addition, these structures exhibited lower solid fractions, which can be critical for applications that require weight reduction.

Chapter 7

General Discussion

The outcomes of the chapter studies in this thesis offer a coherent exploration of how LPBF could change the manufacturing of NiTi SMAs. Through LPBF, the distinct properties of NiTi SMAs, such as SME effects or PE, can be customized for particular applications, thereby opening up new opportunities in the biomedical, aerospace, and industrial domains.

A key research emerging from these studies is the deep influence of LPBF processing parameters (laser power, scanning speed, and hatch spacing) on the actuation properties of SMAs (Chapters 3 and 4). It was found that process parameters modify the resulting microstructure and therefore the phase transformation and thermomechanical behavior of NiTi alloys. These changes were linked with the VED, which directly affects porosity levels, the formation of Ti_2Ni precipitates, and the phase transformation temperatures. The higher the VED, the higher the temperature reached during the AM process. As the temperature increases, the partial pressure of nickel increases more rapidly than for titanium, and therefore nickel becomes more volatile. This preferential Ni evaporation leads to a change in the overall Ni/Ti ratio [199]. As reported in the literature, as lower Ni content higher will be the TTs [86]. Furthermore, no relevant differences were found in the values of Ni evaporation for different VEDs with the selected processing parameters (e.g., laser power, scan speed, or hatch spacing) for the same VED. Microstructural refinement is another critical outcome highlighted in all this study. The ability to fabricate low porosity dense NiTi parts (density $> 99\%$) within a targeted VED range (50-150 J/mm^3) emphasized the reliability of the LPBF process using NiTi alloys.

Furthermore, the higher tendency of Ni to evaporate leads to a local depletion of Ni in the melt pool. Hence, in the absence of nickel, the chance of Ti-rich precipitations to occur, increases. As the molten material solidifies, the remaining Ni and Ti atoms redistribute, sometimes

leading to segregation of Ti-rich regions. The rapid solidification can lead to supersaturation of Ti in the matrix because the equilibrium concentration of Ti in the NiTi phase cannot be maintained due to the fast cooling rates [214] . This supersaturation can drive the nucleation and growth of Ti_2Ni precipitates. These precipitates are formed to reduce the supersaturation of Ti in the NiTi matrix, effectively acting as a sink for the excess of Ti atoms [50]. So, as higher is the VED used to manufacture the NiTi samples higher is the population of Ti_2Ni precipitates.

In addition, the actuation response of the NiTi tensile samples manufactured under different VEDs was studied. It was found that NiTi samples with higher VEDs showed lower recoverable and plastic strains, while the samples manufactured using lower VEDs showed the opposite behavior. The higher population of Ti_2Ni precipitates in the high VED samples affected the actuation response due to they do not undergo any phase transformation and therefore decrease the effective volume of macroscopic deformation [219, 220]. These results open the door to the possibility to tailor the phase transformation and the actuation response in LPBF NiTi SMAs.

Once the effect of the process parameters in the LPBF SMA samples was understood, the next step was to investigate whether the combination of different well-characterized sets of process parameters within a single sample would result in a macroscopic actuation response that reflects the averaged behavior of the individual sets of process parameters or if additional phenomena must be considered to achieve tailored thermomechanical properties (see Chapter 5). To explore these effects, three patterned samples were fabricated using different combinations of previously studied low and high VED sets of process parameters. Each pattern maintained a consistent ratio of the volume processed by each set of process parameters.

The results showed that there was no dependency on the pair of the low and high VED process parameters used for the same patterned sample. However, differences in actuation behavior, including phase transformation and thermomechanical response, were observed between the different patterned geometries. This suggests that non-linear effects arising from the geometric patterns played a key role in influencing the overall thermomechanical behavior.

In the case of the first patterned sample, in which the first half of the sample was manufactured using a high VED parameter and then the other half was manufactured using a low VED parameter, higher recoverable strains in the low VED area were achieved, in contrast to the monoparameter samples manufactured using low VED parameters. It means that probably the effect of manufactured first the high VED parameter produces a higher thermal gradient along the build direction, preferentially orienting the grains of the low VED sites [125] affecting

the overall actuation response [256, 257], obtaining a higher local recoverable strains than the low VED monoparameter samples. This effect also produces a reduction in the plastic strain due to a reduction in the number of grain boundaries [301].

In the cases of the other two patterned samples, the appearance of vertical interfaces introduces higher thermal gradients and defects attributed to the overlapping regions. These regions produce higher Ni evaporation [252] and also an asymmetric manufacturing of the structure, as detailed in Chapter 5. The asymmetric manufacture produces the creation of complex regions that reduce the recoverable strain.in addition, the appearance of other preferential crystallographic orientation during the LPBF process due to the coplex thermal cycles could be responsible for the increase of irrecoverable strains in Pattern 2 after the first thermomechancal cycle [107].

Pattern 3 may exhibit effects similar to those observed in Pattern 2, attributable to the manufacturing method, with both patterns featuring vertical interfaces (refer to Figure 5.1). While Pattern 3 can potentially form different crystal orientations, the expansive central region, produced using a high VED parameter, facilitates the emergence of extensive columnar grains. Furthermore, similar to the behavior observed in monoparameter samples, this central region is expected to contain numerous Ti_2Ni precipitates. Consequently, the overall thermomechanical performance is analogous to that seen in the high VED monoparameter sample.

TTs do not show a specific trend across the patterned geometries. It seems that the introduction of these patterned geometries produce the appearance of complex stress fields and defects during the manufacturing, and they can affect the phase transformation behavior. As the proportion of vertical interfaces increases, so does the overall number of dislocations due to the accumulated heat input [227, 228]. This elevated dislocation density contributes to a reduction in hysteresis behavior. Dislocations facilitate the formation of favorable martensite variants and induce internal stresses, promoting martensitic transformation and influencing TTs in patterned samples. Pattern 3 samples exhibit the lowest A_s values and among the highest M_f values. The hysteresis temperature in the cyclic response of these samples is reduced compared to that of other patterned samples.

Finally, the creation of complex stress fields during the training procedure between the low and high VED regions affect the TWSME effect. The stress fields generated at the interfaces during phase transformation in training cycles hinder the development of new stress fields, thereby preventing the formation of preferential martensite variants, which reduces the TWSME.

It was evident that the vertical interfaces contributed to a degradation of the overall actuation,

while horizontal interfaces facilitated an increase in recoverable strain while reducing plastic deformation. Understanding these non-linear phenomena brings us closer to the possibility of fabricating tailored structures with designed thermomechanical responses. Thus, the final thermomechanical behavior of the sample is influenced not only by the processing parameters but also significantly by the patterned geometry, which plays a crucial role in determining the actuation response.

The latest study in Chapter 6 aimed to integrate the insights gained from research on monoparameters and patterned geometries. But the context was to introduce this knowledge in the creation of lattice structures which can be used as actuators, also taking advantage of their possibilities as the reduction weight and their mechanical properties [271]. To do that, three lattice structures were designed, two of them with all the lattice manufactured using one set of process parameters (one using high VED and other with low VED) and the a third lattice structure built with a combination of process parameters obtaining a graded lattice structure with only horizontal interfaces. The study focused on how process parameters affect the manufacturability of the lattice structures and how these structures behave under a termomechanical stimulus. To do that, the lattice structures were subjected to actuation tests at different loads.

First, the manufacturability of the lattice structures was addressed by measuring the strut diameters and pore sizes produced in the lattice structures. As expected, the high VED set of process parameters produced larger melt pools [249] and therefore higher strut diameters reducing the precision of the printed geometry. The microstructures in the different areas also showed the same results as in the monoparameters samples from the first study obtaining martensitic plates in the low VED areas and large population of Ti_2Ni precipitates in the high VED areas. The same occurred in the graded lattice structure.

As was expected, after the actuation response tests, the lattice manufactured using low VED obtained higher values of recoverable and plastic strains, while the lattice manufactured using high VED parameters obtained the lowest values. In the same line, TTs behaved as expected, obtaining the lowest TTs for the lattice printed using the low VED set of process parameters and the highest TTs for the lattice manufactured using the high VED set of process parameters. In all cases, the graded lattice structure stayed between the other two monoparameter lattice structures. The effect of the interfaces on the graded lattice structure was negligible because of the greater quantity of printed material for each process parameter compared to the monoparameter samples. At this point all the results agreed with the previous studies made.

Computational elastic simulations were performed to demonstrate the effect of the diameter of the strut on the mean stress supported by the beams at the different load levels. This showed that for the same force as higher was the strut diameter, lower was the real stress in the struts. Lattice structures that are identical in design, when fabricated using differing process parameters and exposed to identical loads, experienced varying stress levels within the struts. So, as is well known, there is a stress dependency between the stress level and the total strain in an actuation cycle [194, 284, 285], thereby the results of TTs and the actuation response were averaged using these normalized stress and compared to the previous results of the first study.

Between the phase transformation of lattice structure and bulk material, it was shown how the stress dependence factor changed. This indicates that the loading conditions applied to these structures affect their transformation characteristics. Reedlunn *et al.* [287] thoroughly analyzed how different loading scenarios impact SMAs. They conducted experiments on the same alloy under compression, tension, and bending, revealing distinct responses. They observed that the progression of the transformation frontier in the material varies among tension, compression, and bending loads. Transformation frontiers were more homogeneous under compression, except in regions of buckling. In contrast, during bending, the strain fields showed localized strain primarily on the tensile side, suggesting that some areas in the compression zone did not experience complete transformation by the end of loading. This results in variations in transformation behavior based on the material's loading condition and potentially explains the greater stress dependence found in bulk materials compared to lattice materials. Additionally it was observed by 2D DIC how was the transformation in lattice structures compared to the monoparameter tensile samples. Lattice structures did not show transformation in the external nodes due they were not subjected to any load while the points indicated in the simulation with higher stress concentrations were the first to start the phase transformation.

In this comparison between the tensile samples from the first study and the lattice structures, also it was observed how the lattice structures obtained higher values of recoverable and plastic strains, much higher than the tensile samples in the first study. The paramount aspect is the multiplicative impact of open cell architectures in converting minor microstrains into substantial macroscopic strains within the entire structure. In a uniaxially loaded bulk structure, whether under tension or compression, the local transformation strain translates directly into a macroscopic strain of the same amplitude. In contrast, in scenarios involving non-uniaxially loaded beams, small microstrains may result in significant macrostrains. Traditionally, this mechanism has been used to develop complex geometric configurations

that include various elements for the production of sophisticated SMA actuators [288, 289, 290]. Conversely, in cellular structures, this feature is naturally integrated into the structure's geometry, marked by a combination of multiaxial beam frameworks. The results discussed in this study confirm the considerable potential of additive manufacturing of lattice structures to improve the actuation performance of SMA materials.

The thermomechanical behavior of LPBF NiTi lattice structures is primarily influenced by two significant factors: the geometry of the cell structure and the processing parameters applied at each material point. The cell structure plays a role by affecting various loading scenarios and the manner in which local strains translate into macroscopic strains. Conversely, for a constant cell configuration, the processing parameters affect transformation stresses and temperatures by modulating the microstructure. These results demonstrate a clear synergy derived from the integration of lattice strategies with processing modulation to alter the thermomechanical properties of the SMA. So, the three lattice structures with a BCC unit cell were designed and printed using different parameters, achieving solid fractions between 15–25% and strain recovery values ranging 6–10%. The structures designed in this work exhibit recoverable strains exceeding the ones previously reported NiTi lattice structures. These findings lay the groundwork for an innovative strategy in the crafting of smart ad-hoc shape-memory cellular structures.

In conclusion, the different studies presented illustrate the immense potential of LPBF in advancing NiTi SMA fabrication. By enabling unprecedented control over microstructure and thermomechanical properties, LPBF positions itself as a key technology for creating next-generation metamaterials.

Chapter 8

Conlusions and future work

8.1 Conclusions

This work explores the relationship between the LPBF process parameters and the microstructural, thermomechanical, and functional properties of NiTi SMAs. In addition, it examines the potential for customizing the thermomechanical properties of LPBF NiTi SMAs, which is achieved by local change of the process parameters. The non-linear effect produced by different designs is addressed. The design flexibility offered by the LPBF process leveled up into the fabrication of cellular materials, which, when combined with the capabilities of NiTi, can lead to the creation of unique devices across various industries. The following conclusions were extracted from this work:

- **Processing parameters control the final thermomechanical behavior in homogeneous NiTi samples**: VED is the main factor that influences the porosity, microstructure, phase transformation, and thermomechanical behavior of LPBF NiTi SMAs. Higher VED results in increased nickel evaporation, leading to a greater formation of Ti_2Ni precipitates and higher TTs. The Ti_2Ni precipitates reduce recoverable strain and plastic strain when the samples are exposed to thermal cycles. No significant differences were observed in the achievement of higher VED levels by varying laser power, scanning speed, or hatch spacing, suggesting that VED remains the dominant factor influencing the final material properties, regardless of the specific individual process parameters changed.
- **Digital design of graded NiTi SMA metamaterial by LPBF presents nonlinear phenomena which affect their actuation behavior:** Using spatially con-

trolled LPBF conditions, different patterned geometries were printed to study the effects of the pattern geometry on the thermomechanical behavior. The results demonstrated differing trends, despite the fact that the printed volume for each process parameter set was consistent among the various patterns. This implies that for patterned geometries, the chosen process parameters are not the only responsible for the resulting actuation behavior. The quantity and type of interfaces between the different patterns significantly influence the actuation properties. It need to be taken into account to digitally program the thermomechanical response of NiTi components.

- **Design of NiTi SMA cellular structures with improve functionalities:** NiTi BCC lattice structures were successfully fabricated using LPBF with different process parameters. Higher VED resulted in larger melt pools, reducing printing accuracy, increasing strut diameters, decreasing pore sizes, and increasing solid fractions. Lower VED parameters produced the opposite effects. NiTi lattice structures show ultraelastic behavior with recoverable strains between 6-10%, exceeding traditional bulk NiTi performance. Stress concentration at the edges of the lattice nodes influenced the initiation of phase transformation. The beams undergo full transformation, while the nodes remain unaffected. The designed structures exhibited better recoverable strain performance compared to most documented NiTi lattices, while also maintaining a reduced solid fraction.

This study shows that LPBF technology is an effective method for developing NiTi SMAs, providing exceptional control over their functional properties. By adjusting the local processing parameters and the structural design, the phase transformation temperatures and the thermomechanical properties can be precisely tuned. This capability sets a new path to novel opportunities for creating adaptive and intelligent materials for advanced applications.

8.2 Future Work

The future work available to continue this study falls into the following points:

- **Optimization of LPBF process for improved NiTi properties:** Further research on laser power, scanning speed, and hatch spacing combinations to better control Ni evaporation and, therefore, phase transformation. Investigate real-time monitoring techniques, such as in situ thermography, to optimize process stability and defect reduction.

- **Investigate the effect of other process parameters:** A systematic study can be performed to investigate the influence of the building orientation on the strut geometry and the subsequent effect on thermomecahnical properties, as well as the interaction between the process parameters and different building orientations. In addition, the effect of various scanning strategies on the accuracy of the fabrication and phase transformation could be studied.
- **Deeper investigation on the underlying mechanism of the martensitic transformation:** More detailed research on the transformation mechanisms in the interfaces of patterned geometries is important to localized phase transitions and stress distributions and establish how the interfaces affect the rest of the thermomechanical behavior in the sample. In-situ thermomechanical testing inside SEM can be performed to capture real-time microstructural changes during mechanical loading and thermal cycling. This method allows monitoring the phase transformations and strain.
- **Computational modeling for predictive design:** Improve finite element models to better simulate thermal gradients and stress distributions during the LPBF process which affect the final phase transformations and thermomechanical behavior of the resultant sample. Develop machine learning models trained on LPBF data to predict microstructure evolution and thermomecahnical behavior in NiTi SMAs.
- **Fatigue performance evaluation for industrial applications:** The fatigue behavior of NiTi lattice structures under cyclic loading conditions could be systematically studied to validate their durability in real-world applications. A combination of experimental fatigue testing and in-situ observation techniques (such as X-ray computed tomography) could provide a deeper understanding of crack initiation, defect propagation, and failure mechanisms.
- **Development of functionally graded and multi-material structures:** Future studies could explore the fabrication of functionally graded NiTi structures, where composition and microstructure can be spatially controlled to achieve site-specific mechanical and functional properties. Multi-material printing techniques could also be investigated to integrate NiTi with other metals, expanding the potential applications in different fields.

By addressing these research directions, LPBF NiTi can evolve into a fully tunable and high-performance material platform, unlocking new possibilities for next generation actuators, metamaterials, and structures in multiple industries.

Annexes

A. Supplementary information of the structural simulations of Chapter 5

Stress distribution analysis was performed on the printed geometries through computational finite element analysis (FEA). The geometries patterned under study were meshed using 3D linear tetrahedral elements (C3D4). ABAQUS 2023/Standard software package [248] was used to perform the simulations of the lattice geometries. In terms of boundary conditions, the displacement of the nodes positioned on the lower face of the sample was constrained in all directions through pinned conditions (Ux = Uy = Uz = 0). For nodes located on the upper surface, the displacement was restricted in the X and Y directions (Ux = Uy = 0), while a vertical dipslacement of 0.5 mm was imposed on the Z axis. The constitutive behavior for the material was modeled as perfect elastic-plastic material model with an elastic modulus of 42 GPa and 115 GPa and 150 GPa of yield stress for the low VED and high VED regions respectively. This yield stress was selected using the M_s transformation temperature at a strain of 50% from the total strain of the 200 MPa actuation cycle and then, entering with that temperature in the temperature-stress curve from the results observed in Chapter 4.

B. Supplementary results

Composition (at.%)	Reference	A_s (K)	Recoverable strain (%)
$Ni_{50}Ti_{50}$	[302]	353	6.0
$Ni_{50.5}Ti_{49.5}$	[303]	282	5.8
$Ni_{49.1}Ti_{50.9}$	[303]	275	6.1
$Ni_{51}Ti_{49}$	[302]	184	6.2
$Ni_{50}Ti_{50}$	[302]	270	5.6
$Ni_{50.3}Ti_{49.7}$	[302]	353	3.5
$Ni_{60}Ti_{40}$	[302]	295	1.4
$Ni_{60}Ti_{40}$	[302]	305	2.3
$Ni_{60}Ti_{40}$	[302]	296	1.4
$Ni_{50}Ti_{50}$	[302]	295	5.0
$Ni_{50}Ti_{50}$	[302]	261	2.3
$Ni_{50.8}Ti_{49.2}$	[285]	217	3.3
$Ni_{50}Ti_{50}$	[304]	324	5.2
$Ni_{50}Ti_{50}$	[305]	341	4.1
$Ni_{60}Ti_{40}$	[306]	288	4.5
$Ni_{55}Ti_{45}$	[302]	353	5.8
$Ni_{60}Ti_{40}$	[302]	297	6.0
$Ni_{50}Ti_{50}$	[307]	251	4.5
$Ni_{50}Ti_{50}$	[308]	291	2.9
$Ni_{50.8}Ti_{49.2}$	[309]	281	5.2
$Ni_{50}Ti_{50}$	[310]	239	3.3
$Ni_{50.3}Ti_{49.7}$	[311]	220	3.0

Table 1: Composition, austenite start temperature (A_s) and recoverable strain of NiTi alloys from the literature.

Composition (at.%)	**Reference**	**A_s (K)**	**Recoverable strain (%)**
$Ni_{41}Ti_{49}Cu_{10}$	[303]	307	5.0
$Ni_{41}Ti_{49}Cu_{10}$	[303]	326	5.2
$Ni_{41}Ti_{49}Cu_{10}$	[303]	316	4.7
$Ni_{49.8}Ti_{40.2}Hf_{10}$	[312]	384	4.2
$Ni_{49.8}Ti_{40.7}Hf_{9.5}$	[312]	391	4.7
$Ni_{49.8}Ti_{40.2}Hf_{10}$	[312]	455	1.1
$Ni_{45}Ti_{45}Pt_{10}$	[302]	309	2.5
$Ni_{40}Ti_{50}Pt_{10}$	[302]	246	2.5
$Ni_{34}Ti_{50.5}Pt_{15.5}$	[313]	475	2.5
$Ni_{33.5}Ti_{50.5}Pt_{16}$	[313]	477	2.6
$Ni_{33}Ti_{50.5}Pt_{16.5}$	[313]	495	2.4
$Ni_{20}Ti_{50}Pd_{30}$	[302]	503	-
$Ni_{34.5}Ti_{49.7}Pd_{15.2}$	[302]	348	3.0
$Ni_{29.5}Ti_{49.9}Pd_{20.1}$	[314]	406	2.8
$Ni_{24.4}Ti_{49.6}Pd_{25.2}$	[314]	466	2.5
$Ni_{19.5}Ti_{49.6}Pd_{30.2}$	[314]	523	2.3
$Ni_{3.5}Ti_{49.4}Pd_{46.2}$	[314]	782	-
$Ni_{24.5}Ti_{50.5}Pd_{25}$	[313]	466	-
$Ni_{23.5}Ti_{50.5}Pd_{26}$	[313]	471	-
$Ni_{19.5}Ti_{49.6}Pd_{30.2}$	[315]	523	-
$Ni_{19.4}Ti_{49.6}Pd_{25.2}Au_5$	[315]	512	-
$Ni_{19.6}Ti_{49.2}Pd_{25.3}Pt_{5.1}$	[315]	516	-
$Ni_{47}Ti_{48}Zr_5$	[316]	348	3.2
$Ni_{47}Ti_{43}Zr_{10}$	[316]	386	2.8

Table 2: Composition, austenite start temperature (A_s) and recoverable strain of NiTiCu, NiTiHf, NiTiPt, NiTiPd and NiTiZr alloys from the literature.

Sample ID	P (W)	v (mm/s)	h (µm)	Porosity (%)
1	65	556	56	0.47
2	95	556	81	0.06
3	131	556	112	0.28
4	170	556	145	1.39
5	65	770	40	0.92
6	85	770	53	0.11
7	114	770	70	0.06
8	150	770	93	0.03
9	187	770	116	0.72
10	70	990	34	0.81
11	100	990	48	0.15
12	125	990	60	0.14
13	157	990	76	0.50
14	190	990	91	0.48
15	90	1231	35	0.84
16	125	1231	48	0.09
17	155	1231	60	0.09
18	191	1231	74	0.28
19	228	1231	88	0.52
20	90	1430	30	1.49
21	120	1430	40	1.22
22	154	1430	51	0.05
23	191	1430	64	0.37
24	228	1430	76	0.45
25	80	1650	23	3.93
26	115	1650	33	0.85
27	150	1650	43	0.62
28	191	1650	55	0.32
29	228	1650	66	0.63

Table 3: Process parameter combinations employed to fabricate samples for porosity analysis, resulting in a total VED of 70 J/mm^3 for the broad approach.

Sample ID	P (W)	v (mm/s)	h (µm)	Porosity (%)
1	65	556	49	0.33
2	95	556	71	0.01
3	131	556	98	0.44
4	170	556	127	1.48
5	133	700	79	0.29
6	65	770	35	0.30
7	85	770	46	0.51
8	114	770	62	0.05
9	150	770	81	0.47
10	187	770	101	0.44
11	98	914	45	0.11
12	70	990	29	0.22
13	125	990	52	0.08
14	157	990	66	0.22
15	190	990	80	0.54
16	125	1082	48	0.10
17	175	1100	66	0.40
18	70	1231	24	1.59
19	100	1231	34	0.54
20	155	1231	52	0.11
21	191	1231	65	0.35
22	228	1231	77	0.42
23	134	1235	45	0.04
24	209	1291	67	0.42
25	90	1430	26	0.78
26	120	1430	35	0.55
27	154	1430	45	0.05
28	191	1430	56	0.21
29	228	1430	66	0.40
30	115	1650	29	0.57
31	150	1650	38	0.06
32	191	1650	48	0.32
33	228	1650	58	0.53

Table 4: Process parameter combinations employed to fabricate samples for porosity analysis, resulting in a total VED of 80 J/mm^3 for the broad approach.

Sample ID	P (W)	v (mm/s)	h (µm)	Porosity (%)
1	65	556	43	0.50
2	95	556	63	0.05
3	131	556	87	0.44
4	170	556	113	1.22
5	65	770	31	0.53
6	85	770	40	0.06
7	114	770	54	0.43
8	150	770	72	0.44
9	187	770	90	0.41
10	70	990	26	0.61
11	100	990	37	0.15
12	125	990	48	0.12
13	157	990	59	0.38
14	190	990	71	0.63
15	90	1231	27	0.44
16	120	1231	36	0.42
17	155	1231	47	0.13
18	191	1231	57	0.45
19	228	1231	69	0.49
20	90	1430	23	0.23
21	120	1430	31	0.41
22	150	1430	39	0.04
23	191	1430	49	0.37
24	228	1430	59	0.51
25	80	1650	18	1.65
26	115	1650	26	1.26
27	150	1650	34	0.54
28	191	1650	43	0.05
29	228	1650	51	0.31

Table 5: Process parameter combinations employed to fabricate samples for porosity analysis, resulting in a total VED of 90 J/mm^3 for the broad approach.

Variable	Sample ID	P (W)	v (mm/s)	h (µm)	t (µm)	VED (J/mm^3)
-	Anchor	125	990	48	30	90
Power	P1	72	990	48	30	50
	P2	100	990	48	30	70
	P3	157	990	48	30	110
	P4	185	990	48	30	130
Scan Speed	V1	125	668	48	30	130
	V2	125	869	48	30	100
	V3	125	1082	48	30	80
	V4	125	1231	48	30	70
	V5	125	1739	48	30	50
Hatch Spacing	H1	125	990	28	30	150
	H2	125	990	35	30	120
	H3	125	990	52	30	80
	H4	125	990	60	30	70
	H5	125	990	85	30	50

Table 6: LPBF processing parameters used in the manufacturing of NiTi samples for the systematic approach.

VED (J/mm^3)	Sample ID	M_p (K)	A_p (K)	M_f (K)	M_s (K)	A_s (K)	A_f (K)
70	2	333.4	363.9	317.9	343.5	350.6	373.4
	6	326.9	358.1	310.7	342.7	339.1	373.9
	7	331.1	361.3	315.4	342.5	346.7	374.1
	8	331.9	361.5	314.5	342.1	350.4	372.3
	11	324.5	356.7	309.0	341.0	339.8	367.9
	12	329.8	359.6	313.9	340.0	346.7	369.3
	16	326.3	357.4	309.7	340.9	341.1	368.5
	17	332.2	361.9	313.4	343.3	348.6	374.3
	22	332.2	362.4	315.5	342.3	349.5	372.6
80	2	330.9	361.1	312.3	342.2	345.4	372.3
	8	332.0	361.6	313.6	343.0	347.1	373.0
	11	327.1	358.8	310.3	342.2	342.9	372.1
	13	328.9	359.2	313.6	340.4	346.1	368.8
	16	327.4	358.1	310.6	341.5	343.1	369.3
	20	330.7	362.1	311.0	342.1	348.1	372.7
	27	331.2	362.1	313.9	342.0	348.9	372.3
	31	330.4	361.6	312.2	341.1	348.6	374.4
90	2	330.9	360.8	307.9	342.7	342.5	371.6
	6	328.3	360.0	309.8	342.6	343.8	373.3
	11	329.5	360.3	312.6	343.3	344.0	373.3
	12	329.8	359.6	312.8	339.9	346.7	368.3
	17	332.0	362.3	313.7	342.3	350.0	373.5
	22	332.5	362.6	314.7	342.8	349.0	374.9
	28	332.5	362.1	315.8	343.0	351.5	373.0

Table 7: Transformation temperatures calculated from DSC curves in the broad approach.

Sample	**M_p (K)**	**A_p (K)**	**M_f (K)**	**M_s (K)**	**A_s (K)**	**A_f (K)**
Anchor	330	360	314	341	346	369
P1	323	354	306	340	336	368
P2	325	357	310	340	340	368
P3	335	366	317	345	348	375
P4	336	367	311	347	345	377
V1	335	365	326	346	353	374
V2	334	364	316	345	347	374
V3	327	358	311	341	344	369
V4	326	357	310	340	341	369
V5	329	357	311	340	342	369
H1	335	365	326	345	352	374
H2	336	366	326	345	353	374
H3	329	359	314	340	346	369
H4	330	360	314	340	346	369
H5	330	359	313	340	343	370

Table 8: TTs obtained from the analysis of the DSC curves in Figure 3.8 showing the martensite transformation start temperature (M_s), the martensite transformation finish temperature (M_f), the peak of the martensite transformation (M_p), the austenite start transformation temperature (A_s), the austenite finish transformation temperature (A_f) and the peak of the austenite transformation (A_p) in the systematic approach.

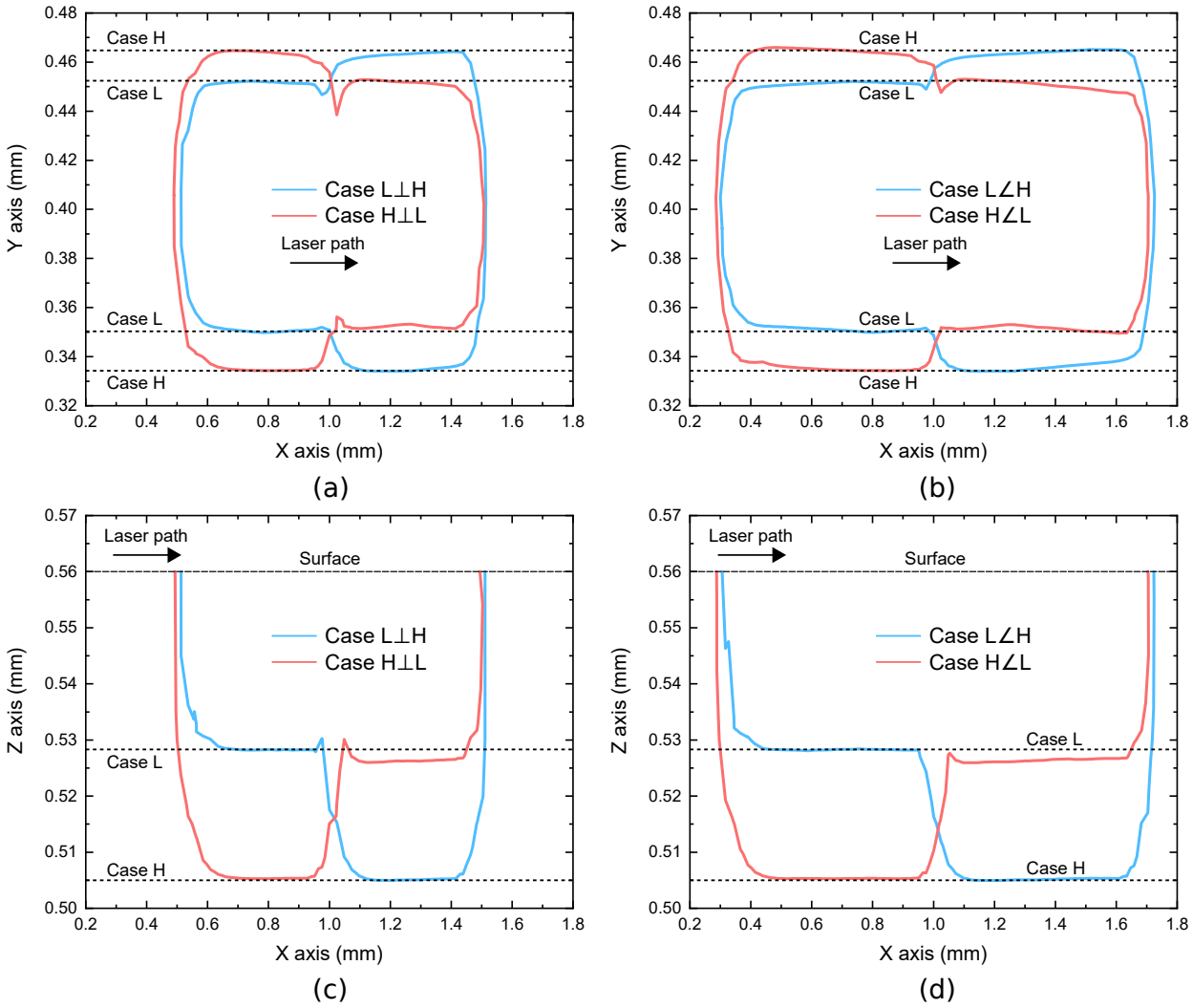

Figure 8.1: Results of the laser track simulations: (a)-(b) display the solid material width and (c)-(d) presents the solid material depth. Cases L and H are presented as dotted lines indicating the maximum values achieved.

References

[1] Dimitris C Lagoudas et al. "Shape memory alloys". In: *Science and Business Media, LLC* (2008).

[2] Darren J Hartl and Dimitris C Lagoudas. "Aerospace applications of shape memory alloys". In: *Proceedings of the Institution of Mechanical Engineers, Part G: Journal of Aerospace Engineering* 221.4 (2007), pp. 535–552. DOI: 10.1243/09544100JAERO211.

[3] L McDonald Schetky. "Shape memory alloy applications in space systems". In: *Materials & Design* 12.1 (1991), pp. 29–32. DOI: 10.1016/0261-3069(91)90089-M.

[4] Donald J Leo et al. "Vehicular applications of smart material systems". In: *Smart structures and materials 1998: Industrial and commercial applications of smart structures technologies*. Vol. 3326. SPIE. 1998, pp. 106–116. DOI: 10.1117/12.310625.

[5] Dieter Stoeckel. "Shape memory actuators for automotive applications". In: *Materials & Design* 11.6 (1990), pp. 302–307. DOI: 10.1016/0261-3069(90)90013-A.

[6] Lorenza Petrini and Francesco Migliavacca. "Biomedical applications of shape memory alloys". In: *Journal of Metallurgy* 2011 (2011). DOI: 10.1155/2011/501483.

[7] Chengli Song. "History and current situation of shape memory alloys devices for minimally invasive surgery". In: *The Open Medical Devices Journal* 2.1 (2010). DOI: 10.2174/1875181401002020024.

[8] Ea Okotete et al. "Shape Memory Nanomaterials for Damping Applications". In: *Handbook of Nanomaterials and Nanocomposites for Energy and Environmental Applications*. Springer, 2020, pp. 1–32. DOI: 10.1007/978-3-030-36268-3_165.

[9] Alain Hautcoeur and Andre Eberhardt. *Eyeglass frame with very high recoverable deformability*. US Patent 5,640,217. June 1997.

[10] Sahar A. Fadlallah et al. "An overview of NiTi shape memory alloy: Corrosion resistance and antibacterial inhibition for dental application". In: *Journal of Alloys and Compounds* 583 (2014). ISSN: 09258388. DOI: 10.1016/j.jallcom.2013.08.029.

[11] Jaronie Mohd Jani et al. *A review of shape memory alloy research, applications and opportunities*. 2014. DOI: 10.1016/j.matdes.2013.11.084.

[12] Mohammad H Elahinia et al. “Manufacturing and processing of NiTi implants: A review”. In: *Progress in materials science* 57.5 (2012), pp. 911–946. DOI: 10.1016/j.pmatsci.2011.11.001.

[13] Yinong Liu, Yong Liu, and Jan Van Humbeeck. “Two-way shape memory effect developed by martensite deformation in NiTi”. In: *Acta materialia* 47.1 (1998), pp. 199–209. DOI: 10.1016/S1359-6454(98)00325-5.

[14] Barsharani Dash et al. “A concise review on machinability of niti shape memory alloys”. In: *Materials Today: Proceedings*. Vol. 18. 2019. DOI: 10.1016/j.matpr.2019.07.511.

[15] Mohammad Elahinia et al. *Fabrication of NiTi through additive manufacturing: A review*. 2016. DOI: 10.1016/j.pmatsci.2016.08.001.

[16] Ali N. Alagha, Shahadat Hussain, and Wael Zaki. *Additive manufacturing of shape memory alloys: A review with emphasis on powder bed systems*. 2021. DOI: 10.1016/j.matdes.2021.109654.

[17] Tomasz Grzegorz Gaweł. “Review of additive manufacturing methods”. In: *Solid State Phenomena* 308 (2020). ISSN: 16629779. DOI: 10.4028/www.scientific.net/SSP.308.1.

[18] Omar Ahmed Mohamed, Syed Hasan Masood, and Wei Xu. “Nickel-titanium shape memory alloys made by selective laser melting: a review on process optimisation”. In: *Advances in Manufacturing* 10 (1 2022). ISSN: 21953597. DOI: 10.1007/s40436-021-00376-9.

[19] Gozde S. Altug-Peduk et al. “Experimental Investigation on the EBM-Based Additively Manufactured Prismatic Nickel–Titanium SMA Components”. In: *Russian Journal of Non-Ferrous Metals* 62 (3 2021). ISSN: 1934970X. DOI: 10.3103/S1067821221030020.

[20] J Frenzel et al. “On the effect of alloy composition on martensite start temperatures and latent heats in Ni–Ti-based shape memory alloys”. In: *Acta Materialia* 90 (2015), pp. 213–231. DOI: 10.1016/j.actamat.2015.02.029.

[21] Y Yang et al. “Laser beam energy dependence of martensitic transformation in SLM fabricated NiTi shape memory alloy”. In: *Materialia* 6 (2019), p. 100305. DOI: 10.1016/j.mtla.2019.100305.

[22] Guangfeng Shi et al. “The interaction effect of process parameters on the phase transformation behavior and tensile properties in additive manufacturing of Ni-rich NiTi alloy”. In: *Journal of Manufacturing Processes* 77 (2022). ISSN: 15266125. DOI: 10.1016/j.jmapro.2022.03.027.

[23] Sasan Dadbakhsh et al. “Laser additive manufacturing of bulk and porous shape-memory NiTi alloys: From processes to potential biomedical applications”. In: *MRS Bulletin* 41 (10 2016). ISSN: 08837694. DOI: 10.1557/mrs.2016.209.

[24] M. Rahim et al. “Impurity levels and fatigue lives of pseudoelastic NiTi shape memory alloys”. In: *Acta Materialia* 61 (10 2013). ISSN: 13596454. DOI: 10.1016/j.actamat.2013.02.054.

[25] Soheil Saedi et al. “On the effects of selective laser melting process parameters on microstructure and thermomechanical response of Ni-rich NiTi”. In: *Acta Materialia* 144 (2018), pp. 552–560. DOI: 10.1016/j.actamat.2017.10.072.

[26] Pan Wang et al. “Experimental analysis of additively manufactured component and design guidelines for lightweight structures: A case study using electron beam melting”. In: *Additive Manufacturing* 33 (2020). ISSN: 22148604. DOI: 10.1016/j.addma.2020.101088.

[27] Ji Ma et al. “Spatial control of functional response in 4D-printed active metallic structures”. In: *Scientific reports* 7.1 (2017), p. 46707. DOI: 10.1038/srep46707.

[28] Mohammadreza Nematollahi et al. “Functionally graded NiTi shape memory alloy: Selective laser melting fabrication and multi-scale characterization”. In: *Materials Letters* 292 (2021). ISSN: 18734979. DOI: 10.1016/j.matlet.2021.129648.

[29] Mohsen Taheri Andani et al. “Mechanical and shape memory properties of porous Ni50.1Ti49.9 alloys manufactured by selective laser melting”. In: *Journal of the Mechanical Behavior of Biomedical Materials* 68 (2017). ISSN: 18780180. DOI: 10.1016/j.jmbbm.2017.01.047.

[30] Arne Ölander. “An electrochemical investigation of solid cadmium-gold alloys”. In: *Journal of the American Chemical Society* 54 (10 1932). ISSN: 15205126. DOI: 10.1021/ja01349a004.

[31] Alden B Greninger and Victor G Mooradian. “Strain transformation in metastable beta copper-zinc and beta copper-Ti alloys”. In: *Aime Trans* 128 (1938), pp. 337–369.

[32] GV Kurdjumov and LG Khandros. “First reports of the thermoelastic behaviour of the martensitic phase of Au-Cd alloys”. In: *Doklady Akademii Nauk SSSR* 66.2 (1949), pp. 211–213.

[33] LC Chang and TA Read. “Behavior of the elastic properties of AuCd”. In: *Trans Met Soc AIME* 191 (1951), p. 47.

[34] GEORGE B. KAUFFMAN and ISAAC MAYO. “The Story of Nitinol: The Serendipitous Discovery of the Memory Metal and Its Applications”. In: *The Chemical Educator* 2 (2 1997). DOI: 10.1007/s00897970111a.

[35] L. Sun et al. *Stimulus-responsive shape memory materials: A review*. 2012. DOI: 10.1016/j.matdes.2011.04.065.

[36] J. P. Oliveira, R. M. Miranda, and F. M. Braz Fernandes. *Welding and Joining of NiTi Shape Memory Alloys: A Review*. 2017. DOI: 10.1016/j.pmatsci.2017.04.008.

[37] Thywill Cephas Dzogbewu and Willie Bouwer du Preez. *Additive manufacturing of ti-based intermetallic alloys: A review and conceptualization of a next-generation machine*. 2021. DOI: 10.3390/ma14154317.

[38] Narges Shayesteh Moghaddam et al. "Anisotropic tensile and actuation properties of NiTi fabricated with selective laser melting". In: *Materials Science and Engineering: A* 724 (2018). ISSN: 09215093. DOI: 10.1016/j.msea.2018.03.072.

[39] Shifeng Wen et al. *Research status and prospect of additive manufactured nickel-titanium shape memory alloys*. 2021. DOI: 10.3390/ma14164496.

[40] Mohsen Attaran. "The rise of 3-D printing: The advantages of additive manufacturing over traditional manufacturing". In: *Business Horizons* 60 (5 2017). ISSN: 00076813. DOI: 10.1016/j.bushor.2017.05.011.

[41] Simon Ford and Mélanie Despeisse. "Additive manufacturing and sustainability: an exploratory study of the advantages and challenges". In: *Journal of Cleaner Production* 137 (2016). ISSN: 09596526. DOI: 10.1016/j.jclepro.2016.04.150.

[42] Zhuoer Chen et al. "Surface roughness of Selective Laser Melted Ti-6Al-4V alloy components". In: *Additive Manufacturing* 21 (2018). ISSN: 22148604. DOI: 10.1016/j.addma.2018.02.009.

[43] Markets and Markets. *Shape Memory Alloy Market by Type (Nitinol, Copper-based, Iron-Manganese-Silicon), End-use Industry (Biomedical, Aerospace Defense, Automotive, Consumer Electronics), and Region - Global Forecast to 2025*. https://www.marketsandmarkets.com/Market-Reports/shape-memory-alloy-market-83856907.html. Accessed: 2025-01-21. 2025.

[44] Zhong Xun Khoo et al. *A review of selective laser melted NiTi shape memory alloy*. 2018. DOI: 10.3390/ma11040519.

[45] H. Meier et al. "Selective laser melting of NiTi shape memory components". In: *Innovative Developments in Design and Manufacturing - Advanced Research in Virtual and Rapid Prototyping*. 2010. DOI: 10.1201/9780203859476-43.

[46] Thywill Cephas Dzogbewu et al. "Supply Chain Disruptions and Resilience in Manufacturing Industry During Covid-19: Additive Manufacturing Intervention in Perspective". In: *Journal of Industrial Engineering and Management* 16 (3 2023). ISSN: 20130953. DOI: 10.3926/jiem.4526.

[47] ASTM Int. "Standard Specification for Wrought Nickel-Titanium Shape Memory Alloys for Medical Devices and Surgical Implants". In: *Annual Book of ASTM Standards* (2012).

[48] Mandaná Moshiri et al. “Benchmarking of laser powder bed fusion machines”. In: *Journal of Manufacturing and Materials Processing* 3 (4 2019). ISSN: 25044494. DOI: 10.3390/jmmp3040085.

[49] Shuaishuai Wei et al. *Laser powder bed fusion additive manufacturing of NiTi shape memory alloys: a review*. 2023. DOI: 10.1088/2631-7990/acc7d9.

[50] Keyvan Safaei et al. “Additive manufacturing of NiTi shape memory alloy for biomedical applications: review of the LPBF process ecosystem”. In: *Jom* (2021), pp. 1–16. DOI: 10.1007/s11837-021-04937-y.

[51] Sasan Dadbakhsh et al. “Effect of SLM parameters on transformation temperatures of shape memory nickel titanium parts”. In: *Advanced Engineering Materials* 16 (9 2014). ISSN: 15272648. DOI: 10.1002/adem.201300558.

[52] Sasan Dadbakhsh et al. “Influence of SLM on shape memory and compression behaviour of NiTi scaffolds”. In: *CIRP annals* 64.1 (2015), pp. 209–212. DOI: 10.1016/j.cirp.2015.04.039.

[53] Hong Zhang, Tao Peng, and Shuangmei Xu. “The influence of scanning pattern on the part properties in powder bed fusion processes: an experimental study”. In: *Procedia CIRP* 61 (2017), pp. 606–611. DOI: 10.1016/j.procir.2016.11.163.

[54] Mehrshad Mehrpouya et al. “A prediction model for finding the optimal laser parameters in additive manufacturing of NiTi shape memory alloy”. In: *International Journal of Advanced Manufacturing Technology* 105 (11 2019). ISSN: 14333015. DOI: 10.1007/s00170-019-04596-z.

[55] Chen Zhang et al. “On the Fabrication of Defect-Free Nickel-Rich Nickel–Titanium Parts Using Laser Powder Bed Fusion”. In: *Journal of Manufacturing Science and Engineering* 144.9 (2022), p. 091011. DOI: 10.1115/1.4054935.

[56] Therese Bormann et al. “Tailoring selective laser melting process parameters for NiTi implants”. In: *Journal of Materials Engineering and Performance* 21 (2012), pp. 2519–2524. DOI: 10.1007/s11665-012-0318-9.

[57] Zhenglei Yu et al. “Prediction of SLM-NiTi transition temperatures based on improved Levenberg–Marquardt algorithm”. In: *Journal of Materials Research and Technology* 15 (2021). ISSN: 22387854. DOI: 10.1016/j.jmrt.2021.09.149.

[58] F. Bartolomeu et al. “Engineering the elastic modulus of NiTi cellular structures fabricated by selective laser melting”. In: *Journal of the Mechanical Behavior of Biomedical Materials* 110 (2020). ISSN: 18780180. DOI: 10.1016/j.jmbbm.2020.103891.

[59] Saghaian SE et al. "Mechanical and shape memory properties of triply periodic minimal surface (TPMS) NiTi structures fabricated by selective laser melting". In: *Biology, Engineering and Medicine* 3 (5 2018). DOI: 10.15761/bem.1000152.

[60] Girolamo Costanza and Maria Elisa Tata. *Shape memory alloys for aerospace, recent developments, and new applications: A short review*. 2020. DOI: 10.3390/MA13081856.

[61] G. F. Andreasen and T. B. Hilleman. "An evaluation of 55 cobalt substituted Nitinol wire for use in orthodontics." In: *Journal of the American Dental Association (1939)* 82 (6 1971). ISSN: 00028177. DOI: 10.14219/jada.archive.1971.0209.

[62] WJ Buehler and RC Wiley. "Nickel-base alloys". In: *Patent Number* (1965).

[63] J Frenzel et al. "Influence of carbon on martensitic phase transformations in NiTi shape memory alloys". In: *Acta materialia* 55.4 (2007), pp. 1331–1341. DOI: 10.1016/j.actamat.2006.10.006.

[64] Darren Hartl et al. "Thermomechanical characterization and modeling of Ni60Ti40 SMA for actuated chevrons". In: *ASME international mechanical engineering congress and exposition*. Vol. 47659. 2006, pp. 281–290.

[65] Kirk Richardson. "Nitinol technologies innovator redefining the cutting edge". In: *Outlook* 22.2 (2001), pp. 1–8.

[66] J Mabe, R Ruggeri, and FT Calkins. "Characterization of nickel-rich nitinol alloys for actuator development". In: *Proceedings of the International Conference on Shape Memory and Superelasticity Technology*. 2006.

[67] Cengiz Tatar, Rauf Acar, and Ibrahim Nazem Qader. "Investigation of thermodynamic and microstructural characteristics of NiTiCu shape memory alloys produced by arc-melting method". In: *European Physical Journal Plus* 135 (3 2020). ISSN: 21905444. DOI: 10.1140/epjp/s13360-020-00288-w.

[68] R. H. Bricknell, K. N. Melton, and O. Mercier. "The structure of NiTiCu shape memory alloys". In: *Metallurgical Transactions A* 10 (6 1979). ISSN: 03602133. DOI: 10.1007/BF02658390.

[69] Toshio Saburi, Youichi Watanabe, and Soji Nenno. "Morphological characteristics of the orthorhombic martensite in a shape memory ti-ni-cu alloy". In: *ISIJ International* 29 (5 1989). ISSN: 09151559. DOI: 10.2355/isijinternational.29.405.

[70] M. Morakabati et al. "Hot tensile properties and microstructural evolution of as cast NiTi and NiTiCu shape memory alloys". In: *Materials and Design* 32 (1 2011). ISSN: 02641275. DOI: 10.1016/j.matdes.2010.05.048.

[71] Tae Hyun Nam, Toshio Saburi, and Ken'ichi Shimizu. "Cu-content dependence of shape memory characteristics in Ti–Ni–Cu alloys". In: *Materials Transactions, JIM* 31.11 (1990), pp. 959–967. DOI: 10.2320/matertrans1989.31.959.

[72] Olivier Mercier and Keith N. Melton. "The substitution of Cu for Ni in NiTi shape memory alloys". In: *Metallurgical Transactions A* 10 (3 1979). ISSN: 03602133. DOI: 10.1007/BF02658353.

[73] O. Karakoc et al. "Actuation fatigue performance of NiTiZr and comparison to NiTiHf high temperature shape memory alloys". In: *Materials Science and Engineering: A* 829 (2022). ISSN: 09215093. DOI: 10.1016/j.msea.2021.142154.

[74] A. Evirgen et al. "Effect of precipitation on the microstructure and the shape memory response of the Ni50.3Ti29.7Zr20 high temperature shape memory alloy". In: *Scripta Materialia* 69 (5 2013). ISSN: 13596462. DOI: 10.1016/j.scriptamat.2013.05.006.

[75] A. Evirgen et al. "Role of nano-precipitation on the microstructure and shape memory characteristics of a new Ni50.3Ti34.7Zr15 shape memory alloy". In: *Materials Science and Engineering: A* 655 (2016). ISSN: 09215093. DOI: 10.1016/j.msea.2015.12.076.

[76] A Evirgen et al. "Microstructural characterization and superelastic response of a Ni50. 3Ti29. 7Zr20 high-temperature shape memory alloy". In: *Scripta Materialia* 81 (2014), pp. 12–15. DOI: 10.1016/j.scriptamat.2014.02.012.

[77] Brian Lin et al. "Structure and thermomechanical behavior of NiTiPt shape memory alloy wires". In: *Acta Biomaterialia* 5 (1 2009). ISSN: 17427061. DOI: 10.1016/j.actbio.2008.07.015.

[78] Thomas W Duerig, KN Melton, and DWCM Stöckel. *Engineering aspects of shape memory alloys*. Butterworth-heinemann, 2013.

[79] KC Atli, I Karaman, and RD Noebe. "Work output of the two-way shape memory effect in Ti50. 5Ni24. 5Pd25 high-temperature shape memory alloy". In: *Scripta Materialia* 65.10 (2011), pp. 903–906. DOI: 10.1016/j.scriptamat.2011.08.006.

[80] Aaron Stebner et al. "Development, characterization, and design considerations of Ni19. 5Ti50. 5 Pd25Pt5 high-temperature shape memory alloy helical actuators". In: *Journal of Intelligent Material Systems and Structures* 20.17 (2009), pp. 2107–2126. DOI: 10.1177/1045389X09347018.

[81] R Noebe, T Biles, and SA Padula. "NiTi-based high-temperature shape-memory alloys: properties, prospects, and potential applications". In: *MATERIALS ENGINEERING-NEW YORK-* 32 (2006), p. 145.

[82] G. S. Firstov, J. Van Humbeeck, and Yu N. Koval. "High temperature shape memory alloys problems and prospects". In: *Journal of Intelligent Material Systems and Structures* 17 (12 2006). ISSN: 1045389X. DOI: 10.1177/1045389X06063922.

[83] Ji Ma, Ibrahim Karaman, and Ronald D Noebe. "High temperature shape memory alloys". In: *International Materials Reviews* 55.5 (2010), pp. 257–315. DOI: 10.1179/095066010X12646898728363.

[84] DR Angst, PE Thoma, and MY Kao. "The effect of hafnium content on the transformation temperatures of Ni49Ti51-xHfx. Shape memory alloys". In: *Journal de physique IV* 5.C8 (1995), pp. C8–747. DOI: 10.1051/jp4/199558747.

[85] B. Kockar et al. "A method to enhance cyclic reversibility of NiTiHf high temperature shape memory alloys". In: *Scripta Materialia* 54 (12 2006). ISSN: 13596462. DOI: 10.1016/j.scriptamat.2006.02.029.

[86] J. Frenzel et al. "Influence of Ni on martensitic phase transformations in NiTi shape memory alloys". In: *Acta Materialia* 58 (9 2010). ISSN: 13596454. DOI: 10.1016/j.actamat.2010.02.019.

[87] H. Shahmir, M. Nili-Ahmadabadi, and F. Naghdi. "Superelastic behavior of aged and thermomechanical treated NiTi alloy at Af+10°C". In: *Materials and Design* 32 (1 2011). ISSN: 02641275. DOI: 10.1016/j.matdes.2010.06.022.

[88] E. Mohammad Sharifi, F. Karimzadeh, and A. Kermanpur. "The effect of cold rolling and annealing on microstructure and tensile properties of the nanostructured Ni50Ti50 shape memory alloy". In: *Materials Science and Engineering: A* 607 (2014). ISSN: 09215093. DOI: 10.1016/j.msea.2014.03.128.

[89] K. F. Hane and T. W. Shield. "Microstructure in the cubic to monoclinic transition in titanium-nickel shape memory alloys". In: *Acta Materialia* 47 (9 1999). ISSN: 13596454. DOI: 10.1016/S1359-6454(99)00143-3.

[90] P. Šittner et al. "R-phase transformation phenomena in thermomechanically loaded NiTi polycrystals". In: *Mechanics of Materials* 38 (5-6 2006). ISSN: 01676636. DOI: 10.1016/j.mechmat.2005.05.025.

[91] H. Morawiec et al. "Two-stage martensitic transformation in a deformed and annealed NiTi alloy". In: *Scripta Materialia* 35 (4 1996). ISSN: 13596462. DOI: 10.1016/1359-6462(96)00179-0.

[92] Yinong Liu and P. G. McCormick. "Thermodynamic analysis of the martensitic transformation in NiTi-I. Effect of heat treatment on transformation behaviour". In: *Acta Metallurgica Et Materialia* 42 (7 1994). ISSN: 09567151. DOI: 10.1016/0956-7151(94)90318-2.

[93] Q. C. Fan et al. "Influence of Ni/Ti ratio and Nb addition on martensite transformation behavior of NiTiNb alloys". In: *Journal of Alloys and Compounds* 790 (2019). ISSN: 09258388. DOI: 10.1016/j.jallcom.2019.02.330.

[94] Kazuhiro Otsuka and Clarence Marvin Wayman. *Shape memory materials*. Cambridge university press, 1999.

[95] Etienne Patoor et al. “Shape memory alloys, Part I: General properties and modeling of single crystals”. In: *Mechanics of Materials* 38 (5-6 2006). ISSN: 01676636. DOI: 10.1016/j.mechmat.2005.05.027.

[96] Bing Wang et al. “Molecular dynamics simulations on one-way shape memory effect of nanocrystalline NiTi shape memory alloy and its cyclic degeneration”. In: *International Journal of Mechanical Sciences* 211 (2021). ISSN: 00207403. DOI: 10.1016/j.ijmecsci.2021.106777.

[97] Bingyao Yan et al. “Martensite twin formation and mechanical properties of B2 austenite NiTi shape memory alloy undergoing severe plastic deformation and subsequent annealing”. In: *Materials Characterization* 178 (2021). ISSN: 10445803. DOI: 10.1016/j.matchar.2021.111273.

[98] Woojin Jeong et al. “Grain scale representative volume element simulation to investigate the effect of crystal orientation on void growth in single and multi-crystals”. In: *Metals* 8 (6 2018). ISSN: 20754701. DOI: 10.3390/met8060436.

[99] Corneliu Cismasiu. *Shape memory alloys*. BoD–Books on Demand, 2010.

[100] K. Otsuka and X. Ren. *Physical metallurgy of Ti-Ni-based shape memory alloys*. 2005. DOI: 10.1016/j.pmatsci.2004.10.001.

[101] Shu Yong Jiang et al. “Influence of Ni4Ti3 precipitates on phase transformation of NiTi shape memory alloy”. In: *Transactions of Nonferrous Metals Society of China (English Edition)* 25 (12 2015). ISSN: 10036326. DOI: 10.1016/S1003-6326(15)64056-0.

[102] J. Kwarciak, Z. Lekston, and H. Morawiec. “Effect of thermal cycling and Ti2Ni precipitation on the stability of the Ni-Ti alloys”. In: *Journal of Materials Science* 22 (7 1987). ISSN: 00222461. DOI: 10.1007/BF01082113.

[103] M. Nishida, C. M. Wayman, and T. Honma. “Precipitation processes in near-equiatomic TiNi shape memory alloys”. In: *Metallurgical Transactions A* 17 (9 1986). ISSN: 03602133. DOI: 10.1007/BF02650086.

[104] K. W.K. Yeung et al. “Optimization of thermal treatment parameters to alter austenitic phase transition temperature of NiTi alloy for medical implant”. In: *Materials Science and Engineering: A* 383 (2 2004). ISSN: 09215093. DOI: 10.1016/j.msea.2004.05.063.

[105] Yufeng Zheng et al. “Effect of ageing treatment on the transformation behaviour of Ti–50.9 at.% Ni alloy”. In: *Acta Materialia* 56.4 (2008), pp. 736–745. DOI: 10.1016/j.actamat.2007.10.020.

[106] E. E. Timofeeva et al. “The superelasticity and shape memory effect in Ni-rich Ti-51.5Ni single crystals after one-step and two-step ageing”. In: *Materials Science and Engineering: A* 796 (2020). ISSN: 09215093. DOI: 10.1016/j.msea.2020.140025.

[107] H Sehitoglu et al. "Shape memory and pseudoelastic behavior of 51.5% Ni–Ti single crystals in solutionized and overaged state". In: *Acta Materialia* 49.17 (2001), pp. 3609–3620. DOI: 10.1016/S1359-6454(01)00216-6.

[108] H. F. Li et al. "Nanocrystalline Ti49.2Ni50.8 shape memory alloy as orthopaedic implant material with better performance". In: *Journal of Materials Science and Technology* 35 (10 2019). ISSN: 10050302. DOI: 10.1016/j.jmst.2019.04.026.

[109] Sheng Li et al. "The development of TiNi-based negative Poisson's ratio structure using selective laser melting". In: *Acta Materialia* 105 (2016). ISSN: 13596454. DOI: 10.1016/j.actamat.2015.12.017.

[110] Mohammad H. Elahinia. *Shape Memory Alloy Actuators: Design, Fabrication and Experimental Evaluation*. 2015. DOI: 10.1002/9781118426913.

[111] J. Alcisto et al. "Tensile properties and microstructures of laser-formed Ti-6Al-4V". In: *Journal of Materials Engineering and Performance* 20 (2 2011). ISSN: 10599495. DOI: 10.1007/s11665-010-9670-9.

[112] Terry Wohlers et al. "History of Additive Manufacturing". In: *SSRN Electronic Journal* (2023). DOI: 10.2139/ssrn.4474824.

[113] William E. Frazier. *Metal additive manufacturing: A review*. 2014. DOI: 10.1007/s11665-014-0958-z.

[114] D. Dev Singh, T. Mahender, and Avala Raji Reddy. "Powder bed fusion process: A brief review". In: *Materials Today: Proceedings*. Vol. 46. 2021. DOI: 10.1016/j.matpr.2020.08.415.

[115] Bonny Onuike, Bryan Heer, and Amit Bandyopadhyay. "Additive manufacturing of Inconel 718—Copper alloy bimetallic structure using laser engineered net shaping (LENS™)". In: *Additive Manufacturing* 21 (2018). ISSN: 22148604. DOI: 10.1016/j.addma.2018.02.007.

[116] Donghong Ding et al. *Wire-feed additive manufacturing of metal components: technologies, developments and future interests*. 2015. DOI: 10.1007/s00170-015-7077-3.

[117] Jan Dutkiewicz et al. "Superelastic Effect in NiTi Alloys Manufactured Using Electron Beam and Focused Laser Rapid Manufacturing Methods". In: *Journal of Materials Engineering and Performance* 29 (7 2020). ISSN: 15441024. DOI: 10.1007/s11665-020-04938-z.

[118] Muhammad Dilawer Hayat et al. "Physical and tensile properties of the NiTi alloy by selective electron beam melting". In: *Key Engineering Materials*. Vol. 770 KEM. 2018. DOI: 10.4028/www.scientific.net/KEM.770.148.

[119] Wengang Zhai et al. “Hybrid manufacturing of -TiAl and Ti–6Al–4V bimetal component with enhanced strength using electron beam melting”. In: *Composites Part B: Engineering* 207 (2021). ISSN: 13598368. DOI: 10.1016/j.compositesb.2020.108587.

[120] Quan Zhou et al. “Selective electron beam melting of NiTi: Microstructure, phase transformation and mechanical properties”. In: *Materials Science and Engineering: A* 744 (2019). ISSN: 09215093. DOI: 10.1016/j.msea.2018.12.023.

[121] L. E. Murr et al. “Characterization of titanium aluminide alloy components fabricated by additive manufacturing using electron beam melting”. In: *Acta Materialia* 58 (5 2010). ISSN: 13596454. DOI: 10.1016/j.actamat.2009.11.032.

[122] Y. J. Liu et al. “Microstructure, defects and mechanical behavior of beta-type titanium porous structures manufactured by electron beam melting and selective laser melting”. In: *Acta Materialia* 113 (2016). ISSN: 13596454. DOI: 10.1016/j.actamat.2016.04.029.

[123] Di Wang et al. *Recent progress on additive manufacturing of multi-material structures with laser powder bed fusion*. 2022. DOI: 10.1080/17452759.2022.2028343.

[124] Zhiwei Xiong et al. “Micro laser powder bed fusion of NiTi alloys with superior mechanical property and shape recovery function”. In: *Additive Manufacturing* 57 (2022). ISSN: 22148604. DOI: 10.1016/j.addma.2022.102960.

[125] Aziz Chniouel et al. “Influence of substrate temperature on microstructural and mechanical properties of 316L stainless steel consolidated by laser powder bed fusion”. In: *International Journal of Advanced Manufacturing Technology* 111 (11-12 2020). ISSN: 14333015. DOI: 10.1007/s00170-020-06316-4.

[126] Lai Chang Zhang and Hooyar Attar. *Selective Laser Melting of Titanium Alloys and Titanium Matrix Composites for Biomedical Applications: A Review*. 2016. DOI: 10.1002/adem.201500419.

[127] Eduard Farber et al. “A review of NiTi shape memory alloy as a smart material produced by additive manufacturing”. In: *Materials Today: Proceedings*. Vol. 30. 2019. DOI: 10.1016/j.matpr.2020.01.563.

[128] Christoph Haberland, Horst Meier, and Jan Frenzel. “On the properties of Ni-rich NiTi shape memory parts produced by selective laser melting”. In: *ASME 2012 Conference on Smart Materials, Adaptive Structures and Intelligent Systems, SMASIS 2012*. Vol. 1. 2012. DOI: 10.1115/SMASIS2012-8040.

[129] J. P. Kruth et al. *Binding mechanisms in selective laser sintering and selective laser melting*. 2005. DOI: 10.1108/13552540510573365.

[130] I. Yadroitsev and I. Smurov. “Surface morphology in selective laser melting of metal powders”. In: *Physics Procedia*. Vol. 12. 2011. DOI: 10.1016/j.phpro.2011.03.034.

[131] I. Yadroitsev, I. Yadroitsava, and I. Smurov. "Strategy of fabrication of complex shape parts based on the stability of single laser melted track". In: *Laser-based Micro- and Nanopackaging and Assembly V*. Vol. 7921. 2011. DOI: 10.1117/12.875402.

[132] Chen Zhang et al. "Processing parameters and martensitic phase transformation relationships in near defect-free additively manufactured NiTiHf high temperature shape memory alloys". In: *Materials and Design* 222 (2022). ISSN: 18734197. DOI: 10.1016/j.matdes.2022.110988.

[133] M. Dallago et al. "Fatigue properties of Ti6Al4V cellular specimens fabricated via SLM: CAD vs real geometry". In: *Procedia Structural Integrity*. Vol. 7. 2017. DOI: 10.1016/j.prostr.2017.11.068.

[134] Jacob C. Snyder and Karen A. Thole. "Understanding laser powder bed fusion surface roughness". In: *Journal of Manufacturing Science and Engineering, Transactions of the ASME* 142 (7 2020). ISSN: 15288935. DOI: 10.1115/1.4046504.

[135] Catalina Jaramillo-Isaza et al. "Correlation of Energy Density and Manufacturing Variables of AA6061 through Laser Powder Bed Fusion and Its Effect on the Densification Mechanism". In: *Metals* 13 (11 2023). ISSN: 20754701. DOI: 10.3390/met13111904.

[136] Minhalina Ahmad Buhairi et al. *Review on volumetric energy density: influence on morphology and mechanical properties of Ti6Al4V manufactured via laser powder bed fusion*. 2023. DOI: 10.1007/s40964-022-00328-0.

[137] Qingchen Deng et al. "Limitations of linear energy density for laser powder bed fusion of Mg-15Gd-1Zn-0.4Zr alloy". In: *Materials Characterization* 190 (2022). ISSN: 10445803. DOI: 10.1016/j.matchar.2022.112071.

[138] E.M. Sequeda Leon et al. "Effect of laser power in laser powder bed fusion on Ni content and structure of Nitinol". In: *Materials Today: Proceedings* (2023). ISSN: 22147853. DOI: 10.1016/j.matpr.2023.05.678.

[139] Y Yang et al. "Evolution of functional properties realized by increasing laser scanning speed for the selective laser melting fabricated NiTi alloy". In: *Journal of Alloys and Compounds* 804 (2019), pp. 220–229. DOI: 10.1016/j.jallcom.2019.06.340.

[140] Narges Shayesteh Moghaddam et al. "Achieving superelasticity in additively manufactured NiTi in compression without post-process heat treatment". In: *Scientific reports* 9.1 (2019), p. 41. DOI: 10.1038/s41598-018-36641-4.

[141] Yuxian Cao et al. "Large tunable elastocaloric effect in additively manufactured Ni–Ti shape memory alloys". In: *Acta Materialia* 194 (2020). ISSN: 13596454. DOI: 10.1016/j.actamat.2020.04.007.

[142] Sayed Ehsan Saghaian et al. "Effect of hatch spacing and laser power on microstructure, texture, and thermomechanical properties of laser powder bed fusion (L-PBF) additively

manufactured NiTi". In: *Optics and Laser Technology* 149 (2022). ISSN: 00303992. DOI: 10.1016/j.optlastec.2021.107680.

[143] Jie Gan et al. "Effect of laser energy density on the evolution of Ni4Ti3 precipitate and property of NiTi shape memory alloys prepared by selective laser melting". In: *Journal of Alloys and Compounds* 869 (2021), p. 159338. DOI: 10.1016/j.jallcom.2021.159338.

[144] L. Xue et al. "Controlling martensitic transformation characteristics in defect-free NiTi shape memory alloys fabricated using laser powder bed fusion and a process optimization framework". In: *Acta Materialia* 215 (2021). ISSN: 13596454. DOI: 10.1016/j.actamat.2021.117017.

[145] Xiebin Wang et al. "Effect of process parameters on the phase transformation behavior and tensile properties of NiTi shape memory alloys fabricated by selective laser melting". In: *Additive Manufacturing* 36 (2020), p. 101545. DOI: 10.1016/j.addma.2020.101545.

[146] Tuhin Mukherjee et al. "Printability of alloys for additive manufacturing". In: *Scientific reports* 6.1 (2016), p. 19717. DOI: 10.1038/srep19717.

[147] Xiebin Wang et al. "Selective laser melting produced layer-structured NiTi shape memory alloys with high damping properties and Elinvar effect". In: *Scripta Materialia* 146 (2018). ISSN: 13596462. DOI: 10.1016/j.scriptamat.2017.11.047.

[148] Xiao Yang et al. "Effect of volume fraction and unit cell size on manufacturability and compressive behaviors of Ni-Ti triply periodic minimal surface lattices". In: *Additive Manufacturing* 54 (2022). ISSN: 22148604. DOI: 10.1016/j.addma.2022.102737.

[149] Carlo Alberto Biffi et al. "Microstructural and mechanical response of NiTi lattice 3D structure produced by selective laser melting". In: *Metals* 10.6 (2020), p. 814. DOI: 10.3390/met10060814.

[150] Saeed Khademzadeh. "Precision additive manufacturing of NiTi shape memory parts using micro-laser powder bed fusion". In: *Progress in Additive Manufacturing* 7.2 (2022), pp. 419–432. DOI: 10.1007/s40964-021-00239-6.

[151] Brian Sanders, Robert Crowe, and Ephrahim Garcia. *Defense advanced research projects agency - Smart materials and structures demonstration program overview*. 2004. DOI: 10.1177/1045389X04042793.

[152] Neeraj Sharma, KamalKumar Jangra, and Tilak Raj. "Applications of Nickel-Titanium Alloy". In: *Journal of Engineering and Technology* 5 (1 2015). ISSN: 0976-8580. DOI: 10.4103/0976-8580.149472.

[153] J. N. Kudva. *Overview of the DARPA smart wing project*. 2004. DOI: 10.1177/1045389X04042796.

[154] Frederick T. Calkins, George W. Butler, and James H. Mabe. "Variable geometry chevrons for jet noise reduction". In: *Collection of Technical Papers - 12th AIAA/CEAS Aeroacoustics Conference*. Vol. 3. 2006. DOI: 10.2514/6.2006-2546.

[155] Silvestro Barbarino et al. *A review of morphing aircraft*. 2011. DOI: 10.1177/1045389X11414084.

[156] J. A. Balta et al. "Embedded shape memory alloys confer aerodynamic profile adaptivity". In: *Smart Materials Bulletin* 2001 (12 2001). ISSN: 14713918. DOI: 10.1016/S1471-3918(01)80094-0.

[157] Justin K. Strelec et al. "Design and implementation of a shape memory alloy actuated reconfigurable airfoil". In: *Journal of Intelligent Material Systems and Structures* 14 (4-5 2003). ISSN: 1045389X. DOI: 10.1177/1045389X03034687.

[158] Raghavendran Mani, Dimitris C. Lagoudas, and Othon K. Rediniotis. "MEMS-based active skin for turbulent drag reduction". In: *Smart Structures and Materials 2003: Smart Structures and Integrated Systems*. Vol. 5056. 2003. DOI: 10.1117/12.483405.

[159] Mohammad Tawfik, Jeng Jong Ro, and Chuh Mei. "Thermal post-buckling and aeroelastic behaviour of shape memory alloy reinforced plates". In: *Smart Materials and Structures* 11 (2 2002). ISSN: 09641726. DOI: 10.1088/0964-1726/11/2/313.

[160] Victor Birman. "Review of mechanics of shape memory alloy structures". In: *Applied Mechanics Reviews* 50 (11 1997). ISSN: 00036900. DOI: 10.1115/1.3101674.

[161] Harsha Prahlad and Inderjit Chopra. "Design of a variable twist tilt-rotor blade using shape memory alloy (SMA) actuators". In: *Smart Structures and Materials 2001: Smart Structures and Integrated Systems*. Vol. 4327. SPIE. 2001, pp. 46–59. DOI: 10.1117/12.436559.

[162] Robert G. Loewy. *Recent developments in smart structures with aeronautical applications*. 1997. DOI: 10.1088/0964-1726/6/5/001.

[163] Claudio Testa et al. "Feasibility study on rotorcraft blade morphing in hovering". In: *Smart Structures and Materials 2005: Smart Structures and Integrated Systems*. Vol. 5764. 2005. DOI: 10.1117/12.600975.

[164] Olivier J. Godard, Magdalini Z. Lagoudas, and Dimitris C. Lagoudas. "Design of space systems using shape memory alloys". In: *Smart Structures and Materials 2003: Smart Structures and Integrated Systems*. Vol. 5056. 2003. DOI: 10.1117/12.483469.

[165] Andrew Peffer et al. "Development and transition of low-shock spacecraft release devices". In: *IEEE Aerospace Conference Proceedings* 4 (2000). ISSN: 1095323X. DOI: 10.1109/AERO.2000.878439.

[166] S.A. Shabalovskaya. "Biological Aspects of TiNi Alloy Surfaces". In: *Journal de Physique IV* 05 (C8 1995). ISSN: 1155-4339. DOI: 10.1051/jp4/1995581199.

[167] Jorma Ryhänen. "Biocompatibility evolution of nickel-titanium shape memory alloy". In: *Academic Dissertation, Faculty of Medicine, University of Oulu, Oulu, Finland* (1999).

[168] M. Simon et al. "A vena cava filter using thermal shape memory alloy: experimental aspects". In: *Radiology* 125 (1 1977). ISSN: 00338419. DOI: 10.1148/125.1.89.

[169] Sanjay Tyagi et al. "Self- and balloon-expandable stent implantation for severe native coarctation of aorta in adults". In: *American Heart Journal* 146 (5 2003). ISSN: 00028703. DOI: 10.1016/S0002-8703(03)00434-4.

[170] Klaus A. Hausegger et al. "Iliac artery stent placement: Clinical experience with a nitinol stent". In: *Radiology* 190 (1 1994). ISSN: 00338419. DOI: 10.1148/radiology.190.1.8259404.

[171] James O. Sanders et al. "A preliminary investigation of shape memory alloys in the surgical correction of scoliosis". In: *Spine* 18 (12 1993). ISSN: 15281159. DOI: 10.1097/00007632-199309000-00012.

[172] L. G. Machado and M. A. Savi. *Medical applications of shape memory alloys*. 2003. DOI: 10.1590/S0100-879X2003000600001.

[173] Sauli Kujala et al. "Bone modeling controlled by a nickel-titanium shape memory alloy intramedullary nail". In: *Biomaterials* 23 (12 2002). ISSN: 01429612. DOI: 10.1016/S0142-9612(01)00388-X.

[174] Michele Coati et al. *Intramedullary nail comprising elements of shape-memory material*. US Patent 8,162,942. Apr. 2012.

[175] T Duerig et al. "Super elastic Nitinol for medical devices-medical plastics and biomaterials, 1997 56". In: *Sandock D et al-Tubular medical prosthesis for use in a body lumen-United States Patent* 5 (), p. 519.

[176] J. S.N. Paine and C. A. Rogers. "High velocity impact response of composites with surface bonded Nitinol-SMA hybrid layers". In: *Collection of Technical Papers - AIAA/ASME/ASCE/AHS/ASC Structures, Structural Dynamics and Materials Conference*. Vol. 3. 1995. DOI: 10.2514/6.1995-1409.

[177] Brian Barnes et al. "Panel deployment using ultrafast SMA latches". In: *ASME International Mechanical Engineering Congress and Exposition*. Vol. 47659. 2006, pp. 273–280. DOI: 10.1115/IMECE2006-15026.

[178] Kazuhiro Otsuka and Tomoyuki Kakeshita. "Science and technology of shape-memory alloys: New developments". In: *MRS Bulletin* 27 (2 2002). ISSN: 08837694. DOI: 10.1557/mrs2002.43.

[179] I Ohkata and Y Suzuki. "The design of shape memory alloy actuators and their applications". In: *Shape memory materials* (1998), pp. 240–266.

[180] Pil-Ho Lee et al. "Dimensional accuracy in additive manufacturing processes". In: *International Manufacturing Science and Engineering Conference*. Vol. 45806. American Society of Mechanical Engineers. 2014, V001T04A045. DOI: 10.1115/MSEC2014-4037.

[181] Hany Hassanin et al. "Surface finish improvement of additive manufactured metal parts". In: *Micro and precision manufacturing* (2018), pp. 145–164. DOI: 10.1007/978-3-319-68801-5_7.

[182] Jason M Walker et al. "Process development and characterization of additively manufactured nickel–titanium shape memory parts". In: *Journal of Intelligent Material Systems and Structures* 27.19 (2016), pp. 2653–2660. DOI: 10.1177/1045389X16635848.

[183] RR Adharapurapu and KS Vecchio. "Superelasticity in a new bioimplant material: Ni-rich 55NiTi alloy". In: *Experimental mechanics* 47 (2007), pp. 365–371. DOI: 10.1007/s11340-006-9004-x.

[184] Soheil Saedi et al. "The influence of heat treatment on the thermomechanical response of Ni-rich NiTi alloys manufactured by selective laser melting". In: *Journal of Alloys and Compounds* 677 (2016), pp. 204–210. DOI: 10.1016/j.jallcom.2016.03.161.

[185] Ronny M Gouveia et al. "Effect of scan strategies and use of support structures on surface quality and hardness of L-PBF AlSi10Mg parts". In: *Materials* 13.10 (2020), p. 2248. DOI: 10.3390/ma13102248.

[186] R Rashid et al. "Effect of energy per layer on the anisotropy of selective laser melted AlSi12 aluminium alloy". In: *Additive Manufacturing* 22 (2018), pp. 426–439. DOI: 10.1016/j.addma.2018.05.040.

[187] Therese Bormann et al. "Microstructure of selective laser melted nickel–titanium". In: *Materials characterization* 94 (2014), pp. 189–202. DOI: 10.1016/j.matchar.2014.05.017.

[188] Jafar Khalil-Allafi, Antonin Dlouhy, and Gunther Eggeler. "Ni4Ti3-precipitation during aging of NiTi shape memory alloys and its influence on martensitic phase transformations". In: *Acta materialia* 50.17 (2002), pp. 4255–4274. DOI: 10.1016/S1359-6454(02)00257-4.

[189] T Simon et al. "On the multiplication of dislocations during martensitic transformations in NiTi shape memory alloys". In: *Acta Materialia* 58.5 (2010), pp. 1850–1860. DOI: 10.1016/j.actamat.2009.11.028.

[190] Yulong Wang et al. "Analysis of internal stresses induced by strain recovery in a single SMA fiber–matrix composite". In: *Composites Part B: Engineering* 42.5 (2011), pp. 1135–1143. DOI: 10.1016/j.compositesb.2011.03.017.

[191] Mohammadreza Nematollahi et al. “Building orientation-structure-property in laser powder bed fusion of NiTi shape memory alloy”. In: *Journal of Alloys and Compounds* 873 (2021), p. 159791. DOI: 10.1016/j.jallcom.2021.159791.

[192] Sasan Dadbakhsh et al. “Texture and anisotropy in selective laser melting of NiTi alloy”. In: *Materials Science and Engineering: A* 650 (2016), pp. 225–232. DOI: 10.1016/j.msea.2015.10.032.

[193] Parisa Bayati et al. “Toward low and high cycle fatigue behavior of SLM-fabricated NiTi: considering the effect of build orientation and employing a self-heating approach”. In: *International Journal of Mechanical Sciences* 185 (2020), p. 105878. DOI: 10.1016/j.ijmecsci.2020.105878.

[194] C. Garrido et al. “On the effect of the processing parameters in microstructure and thermomechanical properties of LPBF NiTi shape memory alloys”. In: *Journal of Materials Research and Technology* 33 (2024), pp. 2414–2429. ISSN: 2238-7854. DOI: 10.1016/j.jmrt.2024.09.155.

[195] Sayed Ehsan Saghaian et al. “Effect of hatch spacing and laser power on microstructure, texture, and thermomechanical properties of laser powder bed fusion (L-PBF) additively manufactured NiTi”. In: *Optics and Laser Technology* 149 (2022). ISSN: 00303992. DOI: 10.1016/j.optlastec.2021.107680.

[196] Zhenglei Yu et al. “Study on properties of SLM-NiTi shape memory alloy under the same energy density”. In: *Journal of Materials Research and Technology* 13 (2021), pp. 241–250. DOI: 10.1016/j.jmrt.2021.04.058.

[197] Hengfeng Gu et al. “Influences of energy density on porosity and microstructure of selective laser melted 17-4PH stainless steel”. In: *24th International SFF Symposium - An Additive Manufacturing Conference, SFF 2013*. 2013.

[198] Pingmei Tang et al. “Numerical analysis of molten pool behavior and spatter formation with evaporation during selective laser melting of 316L stainless steel”. In: *Metallurgical and Materials Transactions B* 50 (2019), pp. 2273–2283. DOI: 10.1007/s11663-019-01641-w.

[199] C. B. Alcock, V. P. Itkin, and M. K. Horrigan. “Vapour pressure equations for the metallic elements: 298-2500k”. In: *Canadian Metallurgical Quarterly* 23 (3 1984). ISSN: 18791395. DOI: 10.1179/cmq.1984.23.3.309.

[200] Matthew Carl et al. “Effect of Ni-content on the transformation temperatures in NiTi-20 at.% Zr high temperature shape memory alloys”. In: *Metals* 7.11 (2017), p. 511. DOI: 10.3390/met7110511.

[201] FL Shen et al. "Effect of energy density on the superelastic property of Ni-rich NiTi alloy fabricated by laser powder bed fusion". In: *Materials Science and Engineering: A* 854 (2022), p. 143874. DOI: 10.1016/j.msea.2022.143874.

[202] Carlo Alberto Biffi et al. "Selective laser melting of NiTi shape memory alloy: processability, microstructure, and superelasticity". In: *Shape Memory and Superelasticity* 6 (2020), pp. 342–353. DOI: 10.1007/s40830-020-00298-8.

[203] Mohammad Elahinia et al. "Additive manufacturing of NiTiHf high temperature shape memory alloy". In: *Scripta Materialia* 145 (2018), pp. 90–94. DOI: 10.1016/j.scriptamat.2017.10.016.

[204] Soheil Saedi et al. "Texture, aging, and superelasticity of selective laser melting fabricated Ni-rich NiTi alloys". In: *Materials Science and Engineering: A* 686 (2017), pp. 1–10. DOI: 10.1016/j.msea.2017.01.008.

[205] HZ Lu et al. "Simultaneous enhancement of mechanical and shape memory properties by heat-treatment homogenization of Ti2Ni precipitates in TiNi shape memory alloy fabricated by selective laser melting". In: *Journal of Materials Science & Technology* 101 (2022), pp. 205–216. DOI: 10.1016/j.jmst.2021.06.019.

[206] DC Ren et al. "Microstructure and properties of equiatomic Ti–Ni alloy fabricated by selective laser melting". In: *Materials Science and Engineering: A* 771 (2020), p. 138586. DOI: 10.1016/j.msea.2019.138586.

[207] HZ Lu et al. "Tailoring phase transformation behavior, microstructure, and superelasticity of NiTi shape memory alloys by specific change of laser power in selective laser melting". In: *Materials Science and Engineering: A* 864 (2023), p. 144576. DOI: 10.1016/j.msea.2022.144576.

[208] Jin Fu et al. "Micro selective laser melting of NiTi shape memory alloy: Defects, microstructures and thermal/mechanical properties". In: *Optics & Laser Technology* 131 (2020), p. 106374. DOI: 10.1016/j.optlastec.2020.106374.

[209] Chaolin Tan et al. "Laser Powder Bed Fusion of Ti-rich TiNi lattice structures: Process optimisation, geometrical integrity, and phase transformations". In: *International Journal of Machine Tools and Manufacture* 141 (2019). ISSN: 08906955. DOI: 10.1016/j.ijmachtools.2019.04.002.

[210] Petr Šittner et al. "Young's modulus of austenite and martensite phases in superelastic NiTi wires". In: *Journal of Materials Engineering and Performance*. Vol. 23. 2014. DOI: 10.1007/s11665-014-0976-x.

[211] R Lahoz and JA Puértolas. "Training and two-way shape memory in NiTi alloys: influence on thermal parameters". In: *Journal of alloys and compounds* 381.1-2 (2004), pp. 130–136. DOI: 10.1016/j.jallcom.2004.03.080.

[212] CL Chu et al. “Fabrication of porous NiTi shape memory alloy for hard tissue implants by combustion synthesis”. In: *Materials Science and Engineering: A* 366.1 (2004), pp. 114–119. DOI: 10.1016/j.msea.2003.08.118.

[213] Naoki Takata et al. “Crystallographic features of microstructure in maraging steel fabricated by selective laser melting”. In: *Metals* 8.6 (2018), p. 440. DOI: 10.3390/met8060440.

[214] J.L. Murray. *Phase diagrams of binary nickel alloys*. Ed. by P. Nash. ASM International, 1991, pp. 342–355.

[215] Yinong Liu and Hong Xiang. “Apparent modulus of elasticity of near-equiatomic NiTi”. In: *Journal of Alloys and Compounds* 270 (1-2 1998). ISSN: 09258388. DOI: 10.1016/S0925-8388(98)00500-3.

[216] MF-X Wagner et al. “Effect of low-temperature precipitation on the transformation characteristics of Ni-rich NiTi shape memory alloys during thermal cycling”. In: *Intermetallics* 18.6 (2010), pp. 1172–1179. DOI: 10.1016/j.intermet.2010.02.048.

[217] Saeed Ataollahi and Mohammad J Mahtabi. “Effects of precipitate on the phase transformation of single-crystal NiTi alloy under thermal and mechanical loads: A molecular dynamics study”. In: *Materials Today Communications* 29 (2021), p. 102859. DOI: 10.1016/j.mtcomm.2021.102859.

[218] Mehrdad Zarinejad, Yong Liu, and Yunxiang Tong. “Transformation temperature changes due to second phase precipitation in NiTi-based shape memory alloys”. In: *Intermetallics* 17.11 (2009), pp. 914–919. DOI: 10.1016/j.intermet.2009.03.022.

[219] Jobin K Joy et al. “Computational Homogenization of Precipitated Shape Memory Alloys: A Comparative Study of FFT Versus FEA”. In: *Shape Memory and Superelasticity* 8.4 (2022), pp. 320–334. DOI: 10.1007/s40830-022-00394-x.

[220] E Hornbogen. “The effect of variables on martensitic transformation temperatures”. In: *Acta Metallurgica* 33.4 (1985), pp. 595–601. DOI: 10.1016/0001-6160(85)90024-0.

[221] Reza Tangestani et al. “An efficient track-scale model for laser powder bed fusion additive manufacturing: Part 1-thermal model”. In: *Frontiers in Materials* 8 (2021), p. 753040. DOI: 10.3389/fmats.2021.753040.

[222] K. C. Atli et al. “Work production using the two-way shape memory effect in NiTi and a Ni-rich NiTiHf high-temperature shape memory alloy”. In: *Smart Materials and Structures* 24 (12 2015). ISSN: 1361665X. DOI: 10.1088/0964-1726/24/12/125023.

[223] K. C. Atli et al. “The effect of training on two-way shape memory effect of binary NiTi and NiTi based ternary high temperature shape memory alloys”. In: *Materials Science and Engineering: A* 560 (2013). ISSN: 09215093. DOI: 10.1016/j.msea.2012.10.009.

[224] Yahui Zhang et al. "Multiscale TRIP-based investigation of low-cycle fatigue of polycrystalline NiTi shape memory alloys". In: *International Journal of Plasticity* 115 (2019). ISSN: 07496419. DOI: 10.1016/j.ijplas.2018.12.003.

[225] A Cox et al. "Predictive modeling of the constitutive response of precipitation hardened Ni-rich NiTi". In: *Shape Memory and Superelasticity* 3 (2017), pp. 9–23. DOI: 10.1007/s40830-016-0096-6.

[226] T. F. Flint et al. "Prediction of grain structure evolution during rapid solidification of high energy density beam induced re-melting". In: *Materials and Design* 147 (2018). ISSN: 18734197. DOI: 10.1016/j.matdes.2018.03.036.

[227] K. M. Bertsch et al. "Origin of dislocation structures in an additively manufactured austenitic stainless steel 316L". In: *Acta Materialia* 199 (2020). ISSN: 13596454. DOI: 10.1016/j.actamat.2020.07.063.

[228] Y. J. Liu et al. "Gradient in microstructure and mechanical property of selective laser melted AlSi10Mg". In: *Journal of Alloys and Compounds* 735 (2018). ISSN: 09258388. DOI: 10.1016/j.jallcom.2017.11.020.

[229] C. H. Fu and Y. B. Guo. "Three-Dimensional Temperature Gradient Mechanism in Selective Laser Melting of Ti-6Al-4V". In: *Journal of Manufacturing Science and Engineering, Transactions of the ASME* 136 (6 2014). ISSN: 15288935. DOI: 10.1115/1.4028539.

[230] Koji Ikuta, Masahiro Tsukamoto, and Shigeo Hirose. "Shape memory alloy servo actuator system with electric resistance feedback and application for active endoscope". In: *Proceedings. 1988 IEEE International Conference on Robotics and Automation*. Ieee. 1988, pp. 427–430. DOI: 10.1109/ROBOT.1988.12085.

[231] Mehrdad Moallem and Vahid Aghazadeh Tabrizi. "Tracking control of an antagonistic shape memory alloy actuator pair". In: *IEEE Transactions on control systems technology* 17.1 (2008), pp. 184–190. DOI: 10.1109/TCST.2008.922506.

[232] T Georges, V Brailovski, and P Terriault. "Characterization and design of antagonistic shape memory alloy actuators". In: *Smart Materials and Structures* 21.3 (2012), p. 035010. DOI: 10.1088/0964-1726/21/3/035010.

[233] André Ianagui and Eduardo Aoun Tannuri. "A sliding mode torque and position controller for an antagonistic SMA actuator". In: *Mechatronics* 30 (2015), pp. 126–139. DOI: 10.1016/j.mechatronics.2015.06.010.

[234] AYN Sofla, DM Elzey, and HNG Wadley. "Two-way antagonistic shape actuation based on the one-way shape memory effect". In: *Journal of Intelligent Material Systems and Structures* 19.9 (2008), pp. 1017–1027. DOI: 10.1177/1045389X07083026.

[235] C Megnin, J Barth, and M Kohl. "A bistable SMA microvalve for 3/2-way control". In: *Sensors and Actuators A: Physical* 188 (2012), pp. 285–291. DOI: 10.1016/j.sna.2011.11.016.

[236] Alaa AbuZaiter et al. "Design and fabrication of a novel XYθz monolithic micro-positioning stage driven by NiTi shape-memory-alloy actuators". In: *Smart Materials and Structures* 25.10 (2016), p. 105004. DOI: 10.1088/0964-1726/25/10/105004.

[237] Farhang Momeni et al. "A review of 4D printing". In: *Materials and Design* 122 (2017). ISSN: 18734197. DOI: 10.1016/j.matdes.2017.02.068.

[238] Shannon E. Bakarich et al. "4D printing with mechanically robust, thermally actuating hydrogels". In: *Macromolecular Rapid Communications* 36 (12 2015). ISSN: 15213927. DOI: 10.1002/marc.201500079.

[239] Cheng Lin et al. "4D printing of personalized shape memory polymer vascular stents with negative Poisson's ratio structure: A preliminary study". In: *Science China Technological Sciences* 63 (4 2020). ISSN: 18691900. DOI: 10.1007/s11431-019-1468-2.

[240] Bo Cheng et al. "On Process Temperature in Powder-Bed Electron Beam Additive Manufacturing: Model Development and Validation". In: *Journal of Manufacturing Science and Engineering, Transactions of the ASME* 136 (6 2014). ISSN: 15288935. DOI: 10.1115/1.4028484.

[241] Ming Liu et al. "A characteristic time-based heat input model for simulating selective laser melting". In: *Additive Manufacturing* 44 (2021). ISSN: 22148604. DOI: 10.1016/j.addma.2021.102026.

[242] Jia Ning Zhu et al. "Controlling microstructure evolution and phase transformation behavior in additive manufacturing of nitinol shape memory alloys by tuning hatch distance". In: *Journal of Materials Science* 57 (10 2022). ISSN: 15734803. DOI: 10.1007/s10853-022-07007-z.

[243] C. Zanotti et al. "Comparison between the thermal properties of fully dense and porous NiTi SMAs". In: *Intermetallics* 18 (1 2010). ISSN: 09669795. DOI: 10.1016/j.intermet.2009.06.001.

[244] Khashayar Khanlari et al. "Fabrication of Ni-Rich 58NiTi and 60NiTi from Elementally Blended Ni and Ti Powders by a Laser Powder Bed Fusion Technique: Their Printing, Homogenization and Densification". In: *International Journal of Molecular Sciences* 23 (16 2022). ISSN: 14220067. DOI: 10.3390/ijms23169495.

[245] Hiroyuki Kato. "Latent heat storage capacity of NiTi shape memory alloy". In: *Journal of Materials Science* 56 (13 2021). ISSN: 15734803. DOI: 10.1007/s10853-021-05777-6.

[246] J. Gibkes et al. “Local influence of material processing on phase transitions in NiTi shape memory alloys investigated by IR thermography”. In: *Materials Science and Engineering: A* 378 (1-2 SPEC. ISS. 2004). ISSN: 09215093. DOI: 10.1016/j.msea.2003.10.343.

[247] Emrecan Soylemez. “High deposition rate approach of selective laser melting through defocused single bead experiments and thermal finite element analysis for Ti-6Al-4V”. In: *Additive Manufacturing* 31 (2020). ISSN: 22148604. DOI: 10.1016/j.addma.2019.100984.

[248] Dassault Systemes. *ABAQUS 2023 Documentation*. Available at: https://www.3ds.com/products-services/simulia/products/abaqus/. Dassault Systemes Simulia Corp. Providence, RI, USA, 2023.

[249] Sampreet Rangaswamy et al. “Investigating Melt Pool Dimensions in Laser Powder Bed Fusion of Nitinol: An Analytical Approach”. In: *Advanced Engineering Materials* (2024), p. 2401636. DOI: 10.1002/adem.202401636.

[250] T. Zakrzewski et al. “Dimensional analysis of the effect of SLM parameters on surface roughness and material density”. In: *Procedia CIRP*. Vol. 95. 2020. DOI: 10.1016/j.procir.2020.01.182.

[251] H. Z. Lu et al. “Altered phase transformation behaviors and enhanced bending shape memory property of NiTi shape memory alloy via selective laser melting”. In: *Journal of Materials Processing Technology* 303 (2022). ISSN: 09240136. DOI: 10.1016/j.jmatprotec.2022.117546.

[252] Zheng Xiang et al. “Tensile mechanical behavior of functionally graded NiTi alloy manufactured via laser powder bed fusion”. In: *Materials Science and Engineering: A* 914 (2024), p. 147119. DOI: 10.1016/j.msea.2024.147119.

[253] Jeff Perkins and Darel Hodgson. “The two-way shape memory effect”. In: *Engineering aspects of shape memory alloys* (1990), pp. 195–206.

[254] Keyvan Safaei et al. “Controlling texture of NiTi alloy processed by laser powder bed fusion: Smart build orientation and scanning strategy”. In: *Additive Manufacturing Letters* 5 (2023). ISSN: 27723690. DOI: 10.1016/j.addlet.2023.100126.

[255] Takuya Ishimoto et al. “Stability of crystallographic texture in laser powder bed fusion: Understanding the competition of crystal growth using a single crystalline seed”. In: *Additive Manufacturing* 43 (2021). ISSN: 22148604. DOI: 10.1016/j.addma.2021.102004.

[256] T. Waitz, V. Kazykhanov, and H. P. Karnthaler. “Martensitic phase transformations in nanocrystalline NiTi studied by TEM”. In: *Acta Materialia* 52 (1 2004). ISSN: 13596454. DOI: 10.1016/j.actamat.2003.08.036.

[257] Bo Xu, Chong Wang, and Qingyuan Wang. "Toward tunable shape memory effect of NiTi alloy by grain size engineering: A phase field study". In: *Journal of Materials Science and Technology* 168 (2024). ISSN: 10050302. DOI: 10.1016/j.jmst.2022.10.089.

[258] C Urbina et al. "New understanding of the influence of the pre-training phase transformation behaviour on the TWSME in NiTi SMA wires". In: *Experimental Mechanics* 53 (2013), pp. 1415–1436. DOI: 10.1007/s11340-013-9756-z.

[259] F. Auricchio, S. Marfia, and E. Sacco. "Modelling of SMA materials: Training and two way memory effects". In: *Computers and Structures* 81 (24-25 2003). ISSN: 00457949. DOI: 10.1016/S0045-7949(03)00319-5.

[260] Ling Qiu, Zijun He, and Dan Li. "Multifunctional Cellular Materials Based on 2D Nanomaterials: Prospects and Challenges". In: *Advanced Materials* 30 (4 2018). ISSN: 15214095. DOI: 10.1002/adma.201704850.

[261] Dhruv Bhate et al. *Classification and selection of cellular materials in mechanical design: Engineering and biomimetic approaches*. 2019. DOI: 10.3390/designs3010019.

[262] Chen Pan, Yafeng Han, and Jiping Lu. *Design and optimization of lattice structures: A review*. 2020. DOI: 10.3390/APP10186374.

[263] Zhijun Zheng et al. "Dynamic stress-strain states for metal foams using a 3D cellular model". In: *Journal of the Mechanics and Physics of Solids* 72 (2014). ISSN: 00225096. DOI: 10.1016/j.jmps.2014.07.013.

[264] MF Ashby. *Metal Foams: a design guide*. Butterworth-Heinemann College, 2000.

[265] J. Zhang and M. F. Ashby. "The out-of-plane properties of honeycombs". In: *International Journal of Mechanical Sciences* 34 (6 1992). ISSN: 00207403. DOI: 10.1016/0020-7403(92)90013-7.

[266] Yunlong Tang and Yaoyao Fiona Zhao. "A survey of the design methods for additive manufacturing to improve functional performance". In: *Rapid Prototyping Journal* 22.3 (2016), pp. 569–590. DOI: 10.1108/RPJ-01-2015-0011.

[267] R Rezaei et al. "Mechanical characterization and finite element modeling of polylactic acid BCC-Z cellular lattice structures fabricated by fused deposition modeling". In: *Proceedings of the Institution of Mechanical Engineers, Part C: Journal of Mechanical Engineering Science* 231.11 (2017), pp. 1995–2004. DOI: 10.1177/0954406215626941.

[268] Fergal J. O'Brien. *Biomaterials scaffolds for tissue engineering*. 2011. DOI: 10.1016/S1369-7021(11)70058-X.

[269] Michele Bici et al. "Development of a multifunctional panel for aerospace use through SLM additive manufacturing". In: *Procedia CIRP*. Vol. 67. 2018. DOI: 10.1016/j.procir.2017.12.202.

[270] Trac D. Tran. "Linear-Phase Perfect Reconstruction Filter Bank: Lattice Structure, Design, and Application in Image Coding". In: *IEEE Transactions on Signal Processing* 46 (9 1998). ISSN: 1053587X.

[271] Tobias Maconachie et al. *SLM lattice structures: Properties, performance, applications and challenges*. 2019. DOI: 10.1016/j.matdes.2019.108137.

[272] Yash Agrawal and G. K. Ananthasuresh. "Towards optimal heterogeneity in lattice structures". In: *Structural and Multidisciplinary Optimization* 64 (4 2021). ISSN: 16151488. DOI: 10.1007/s00158-021-03003-0.

[273] Parastoo Jamshidi et al. "Development, characterisation, and modelling of processability of nitinol stents using laser powder bed fusion". In: *Journal of Alloys and Compounds* 909 (2022). ISSN: 09258388. DOI: 10.1016/j.jallcom.2022.164681.

[274] Tobias Gustmann et al. "Properties of a superelastic NiTi shape memory alloy using laser powder bed fusion and adaptive scanning strategies". In: *Progress in Additive Manufacturing* 5 (1 2020). ISSN: 23639520. DOI: 10.1007/s40964-020-00118-6.

[275] DICe Developers. *Digital Image Correlation Engine (DICe)*. 2024. URL: https://github.com/dicengine/dice.

[276] K. S. Suresh et al. "Microstructure dependent elastic modulus variation in NiTi shape memory alloy". In: *Journal of Alloys and Compounds* 633 (2015). ISSN: 09258388. DOI: 10.1016/j.jallcom.2015.01.301.

[277] Massimiliano Casata et al. "A holistic study of the effect of geometrical and processing conditions on the static mechanical performance of LPBF strut elements". In: *Materials & Design* 247 (2024), p. 113387. DOI: 10.1016/j.matdes.2024.113387.

[278] Chunze Yan et al. "Evaluations of cellular lattice structures manufactured using selective laser melting". In: *International Journal of Machine Tools and Manufacture* 62 (2012). ISSN: 08906955. DOI: 10.1016/j.ijmachtools.2012.06.002.

[279] Simon Van Bael et al. "Micro-CT-based improvement of geometrical and mechanical controllability of selective laser melted Ti6Al4V porous structures". In: *Materials Science and Engineering: A* 528.24 (2011), pp. 7423–7431. DOI: 10.1016/j.msea.2011.06.045.

[280] Edwin B Glaubitz et al. "Contour parameters, melt pool behavior, and surface roughness relationships across laser powder bed fusion platforms and metallic alloys". In: *The International Journal of Advanced Manufacturing Technology* (2025), pp. 1–19. DOI: 10.1007/s00170-025-15066-0.

[281] Nikolas W. Hrabe et al. "Compression-compression fatigue of selective electron beam melted cellular titanium (Ti-6Al-4V)". In: *Journal of Biomedical Materials Research*

- *Part B Applied Biomaterials* 99 B (2 2011). ISSN: 15524973. DOI: 10.1002/jbm.b.31901.

[282] XY Cheng et al. "Compression deformation behavior of Ti–6Al–4V alloy with cellular structures fabricated by electron beam melting". In: *Journal of the mechanical behavior of biomedical materials* 16 (2012), pp. 153–162. DOI: 10.1016/j.jmbbm.2012.10.005.

[283] Liang Xing Lu et al. "Integrated modelling and simulation of NiTi alloy by powder bed fusion: Single track study". In: *Materials and Design* 227 (2023). ISSN: 18734197. DOI: 10.1016/j.matdes.2023.111755.

[284] D. J. Hartl et al. "Use of a Ni60Ti shape memory alloy for active jet engine chevron application: I. thermomechanical characterization". In: *Smart Materials and Structures* 19 (1 2010). ISSN: 09641726. DOI: 10.1088/0964-1726/19/1/015020.

[285] Dimitris Lagoudas et al. "Constitutive model for the numerical analysis of phase transformation in polycrystalline shape memory alloys". In: *International Journal of Plasticity* 32-33 (2012). ISSN: 07496419. DOI: 10.1016/j.ijplas.2011.10.009.

[286] Wenqian Guo et al. "Effect of laser scanning speed on the microstructure, phase transformation and mechanical property of NiTi alloys fabricated by LPBF". In: *Materials and Design* 215 (2022). ISSN: 18734197. DOI: 10.1016/j.matdes.2022.110460.

[287] Benjamin Reedlunn et al. "Tension, compression, and bending of superelastic shape memory alloy tubes". In: *Journal of the Mechanics and Physics of Solids* 63 (1 2014). ISSN: 00225096. DOI: 10.1016/j.jmps.2012.12.012.

[288] Qiang Liu, Sepideh Ghodrat, and Kaspar M.B. Jansen. "Modelling and mechanical design of a flexible tube-guided SMA actuator". In: *Materials and Design* 216 (2022). ISSN: 18734197. DOI: 10.1016/j.matdes.2022.110571.

[289] Qiang Liu et al. *Shape memory alloy actuators for haptic wearables: A review*. 2023. DOI: 10.1016/j.matdes.2023.112264.

[290] Hussein F.M. Ali and Youngshik Kim. "Design procedure and control of a small-scale knee exoskeleton using shape memory alloy springs". In: *Microsystem Technologies* 29 (8 2023). ISSN: 14321858. DOI: 10.1007/s00542-023-05499-6.

[291] Nathan J. Bechle and Stelios Kyriakides. "Localization in NiTi tubes under bending". In: *International Journal of Solids and Structures* 51 (5 2014). ISSN: 00207683. DOI: 10.1016/j.ijsolstr.2013.11.023.

[292] Ken Gall et al. "Tension–compression asymmetry of the stress–strain response in aged single crystal and polycrystalline NiTi". In: *Acta Materialia* 47.4 (1999), pp. 1203–1217. DOI: 10.1016/S1359-6454(98)00432-7.

[293] Keyvan Safaei Baghbaderani et al. "Mechanical evaluation of selective laser melted Ni-rich NiTi: Compression, Tension, and Torsion". In: *ASME 2020 15th International Manufacturing Science and Engineering Conference, MSEC 2020*. Vol. 1. 2020. DOI: 10.1115/MSEC2020-8432.

[294] Zhaorui Yan et al. "Superelastic response and damping behavior of additively manufactured Nitinol architectured materials". In: *Additive Manufacturing* 68 (2023). ISSN: 22148604. DOI: 10.1016/j.addma.2023.103505.

[295] Dohyung Kim et al. "3D and 4D Printing of Complex Structures of Fe-Mn-Si-Based Shape Memory Alloy Using Laser Powder Bed Fusion". In: *Advanced Materials Interfaces* 9 (13 2022). ISSN: 21967350. DOI: 10.1002/admi.202200171.

[296] H. Z. Lu et al. "Microstructure, shape memory properties, and in vitro biocompatibility of porous NiTi scaffolds fabricated via selective laser melting". In: *Journal of Materials Research and Technology* 15 (2021). ISSN: 22387854. DOI: 10.1016/j.jmrt.2021.11.112.

[297] Wenliang Chen et al. "Compression Behavior of Graded NiTi Gyroid-Structures Fabricated by Laser Powder Bed Fusion Additive Manufacturing Under Monotonic and Cyclic Loading". In: *JOM* 73 (12 2021). ISSN: 15431851. DOI: 10.1007/s11837-021-04938-x.

[298] M. R. Karamooz Ravari et al. "On the effects of geometry, defects, and material asymmetry on the mechanical response of shape memory alloy cellular lattice structures". In: *Smart Materials and Structures* 25 (2 2016). ISSN: 1361665X. DOI: 10.1088/0964-1726/25/2/025008.

[299] Lingqi Sun et al. "Mechanical and shape memory properties of NiTi triply periodic minimal surface structures fabricated by laser powder bed fusion". In: *Journal of Manufacturing Processes* 101 (2023). ISSN: 15266125. DOI: 10.1016/j.jmapro.2023.06.034.

[300] Xin Liu et al. "Topological optimisation and laser additive manufacturing of force-direction-sensitive NiTi porous structures with large deformation recovery behaviour". In: *Virtual and Physical Prototyping* 19.1 (2024), e2365860. DOI: 10.1080/17452759.2024.2365860.

[301] Tomohito TSURU et al. "Atomistic Simulations of Stress Concentration and Dislocation Nucleation at Grain Boundaries". In: *Progress in Nuclear Science and Technology* 2 (0 2011). ISSN: 2185-4823. DOI: 10.15669/pnst.2.20.

[302] D Hartl and D Lagoudas. *Shape memory alloys: modeling and engineering applications*. 2008.

[303] Bohumír Strnadel et al. “Cyclic stress-strain characteristics of Ti Ni and Ti Ni Cu shape memory alloys”. In: *Materials Science and Engineering: A* 202.1-2 (1995), pp. 148–156. DOI: 10.1016/0921-5093(95)09801-1.

[304] DANIELA RIGAMONTI and FRANCESCO ZANETTI. “Design and characterisation of shape memory alloys for optomechanical mountings”. In: (2010).

[305] H. Sayyaadi, M. R. Zakerzadeh, and H. Salehi. “A comparative analysis of some one-dimensional shape memory alloy constitutive models based on experimental tests”. In: *Scientia Iranica* 19 (2 2012). ISSN: 10263098. DOI: 10.1016/j.scient.2012.01.005.

[306] Darren J. Hartl et al. “Experimentally validated numerical analysis of aerostructures incorporating shape memory alloys”. In: *Behavior and Mechanics of Multifunctional and Composite Materials 2008*. Vol. 6929. 2008. DOI: 10.1117/12.776356.

[307] Michele Conti et al. “Nitinol embolic protection filters: Design investigation by finite element analysis”. In: *Journal of Materials Engineering and Performance* 18 (5-6 2009). ISSN: 10599495. DOI: 10.1007/s11665-009-9408-8.

[308] F. Farzin-Nia and T. Yoneyama. “Orthodontic devices using Ti-Ni shape memory alloys”. In: 2008. DOI: 10.1533/9781845695248.2.257.

[309] D. Favier et al. “Influence of thermomechanical processing on the superelastic properties of a Ni-rich Nitinol shape memory alloy”. In: *Materials Science and Engineering: A* 429 (1-2 2006). ISSN: 09215093. DOI: 10.1016/j.msea.2006.05.018.

[310] Biagio Carboni, Walter Lacarbonara, and Ferdinando Auricchio. “Hysteresis of Multi-configuration Assemblies of Nitinol and Steel Strands: Experiments and Phenomenological Identification”. In: *Journal of Engineering Mechanics* 141 (3 2015). ISSN: 0733-9399. DOI: 10.1061/(asce)em.1943-7889.0000852.

[311] A. Jalaeefar and B. Asgarian. “Experimental Investigation of Mechanical Properties of Nitinol, Structural Steel, and Their Hybrid Component”. In: *Journal of Materials in Civil Engineering* 25 (10 2013). ISSN: 0899-1561. DOI: 10.1061/(asce)mt.1943-5533.0000701.

[312] P. L. Potapov et al. “Effect of Hf on the structure of Ni-Ti martensitic alloys”. In: *Materials Letters* 32 (4 1997). ISSN: 0167577X. DOI: 10.1016/S0167-577X(97)00037-2.

[313] Jordan E. Massad et al. “High-temperature superelasticity in NiTiPt and NiTiPd shape memory alloys”. In: *Journal of Intelligent Material Systems and Structures* 34 (4 2023). ISSN: 15308138. DOI: 10.1177/1045389X221105885.

[314] Glen S. Bigelow et al. “Characterization of ternary NiTiPd high-temperature shape-memory alloys under load-biased thermal cycling”. In: *Metallurgical and Materials*

Transactions A: Physical Metallurgy and Materials Science 41 (12 2010). ISSN: 10735623. DOI: 10.1007/s11661-010-0365-5.

[315] GIen Bigelow et al. "Development and characterization of improved nitipd high-temperature shape-memory alloys by solid-solution strengthening and thermomechanical processing". In: *SMST-2006 - Proceedings of the International Conference on Shape Memory and Superelastic Technologies*. 2008. DOI: 10.1361/cp2006smst113.

[316] SF Hsieh and SK Wu. "Martensitic transformation of quaternary Ti50. 5- XNi49. 5ZrX/2HfX/2 (X= 0–20 at.%) shape memory alloys". In: *Materials characterization* 45.2 (2000), pp. 143–152. DOI: 10.1016/S1044-5803(00)00068-1.